

# Eliminating TRF-related System Errors Through Recursive TRF Realization Strategy for the CMONOC GPS Stations

**weiwei wu**

Institute of Earthquake Forecasting China Earthquake Administration

**Guojie Meng** (✉ [mgj@ief.ac.cn](mailto:mgj@ief.ac.cn))

Institute of Earthquake Forecasting, China Earthquake Administration, Beijing, 100036, China.

<https://orcid.org/0000-0002-6584-0380>

**Jicang Wu**

College of Surveying and Geo-Informatics, Tongji University

**Guoqiang Zhao**

Institute of Earthquake Forecasting China Earthquake Administration

---

**Full paper**

**Keywords:** Recursive TRF realization, TRF-related system errors, CMONOC, RMS

**Posted Date:** December 17th, 2020

**DOI:** <https://doi.org/10.21203/rs.3.rs-127452/v1>

**License:**  This work is licensed under a Creative Commons Attribution 4.0 International License.

[Read Full License](#)

---

# 1 **Eliminating TRF-related system errors through recursive TRF**

## 2 **Realization strategy for the CMONOC GPS stations**

3  
4 **Weiwei Wu<sup>1,2</sup>, Guojie Meng<sup>1\*,2</sup>, Jicang Wu<sup>3</sup>, Guoqiang Zhao<sup>1,2</sup>**

5 1. Key Laboratory of Earthquake Prediction, China Earthquake Administration,  
6 Beijing, 100036, China; [wwei@ief.ac.cn](mailto:wwei@ief.ac.cn), [mgj@ief.ac.cn](mailto:mgj@ief.ac.cn), , [gqzhao@ief.ac.cn](mailto:gqzhao@ief.ac.cn).

7 2. Institute of Earthquake Forecasting, China Earthquake Administration, Beijing,  
8 100036, China.

9 3. College of Surveying and Geo-Informatics, Tongji University, Shanghai, 200092,  
10 China; [jcwu@tongji.edu.cn](mailto:jcwu@tongji.edu.cn).

### 11 12 **Abstract**

13 It is vital in the study of crustal deformation to reduce system errors and enhance  
14 the accuracy of GPS coordinate time series. To eliminate system errors associated in  
15 the coordinate time series, which are related to the terrestrial reference frame (TRF)  
16 realization, we develop a recursive TRF realization strategy in regional GPS data  
17 processing. We have processed the whole set of CMONOC (Crustal Movement  
18 Observation Network of China) GPS data by the Bernese software, and employ the  
19 controlled datum removal (CDR) filter to solve the rank defect problem in the daily  
20 coordinate normal equations. On the recursive TRF realization of stations' coordinates,  
21 we iteratively perform time series modeling with integral trajectory models, TRF  
22 realization with all continuous stations treated as "pseudo" fiducial stations, and  
23 frame alignment to the ITRF2014 with the 6-parameters Helmert transformation. We  
24 obtain the final coordinate time series through 3 times of iterations for the CMONOC  
25 data. Compared to the results derived from the conventional TRF realization strategy  
26 with the average root mean squares (RMS) being 1.98mm, 2.62 mm and 5.39 mm for  
27 east, north and up components, respectively, the average RMS earn significant  
28 reduction up to 30%, 43% and 16% in the first loop, with their quantities being 1.41  
29 mm, 1.51 mm and 4.57 mm for east, north and up components, respectively, and

30 negligible changes in the following 2 loops. In contrast to previous studies, our strategy  
31 is feasible in the processing of regional geodetic networks, and is concentrated on the  
32 TRF-related system errors without any pre-assumption and spatial limitation. In  
33 essence, our recursive strategy is to tighten the constraints for the CMONOC GPS  
34 stations in the TRF realization through the leaning of the barycenter of the processed  
35 geodetic network, thus inevitably loosening the constraints for other globally  
36 distributed stations, and slightly magnifying their RMS. On the whole, the north  
37 component of coordinates time series has a maximum RMS reduction, resulting in  
38 identical precision for both horizontal components, thus indicating that our strategy  
39 remedies the frame defects stemming from the extremely uneven distribution of the  
40 reference network, and retrieves the “real” precision of GPS observations. The  
41 insignificant RMS reduction on the vertical component may be attributed to insufficient  
42 time series modeling. Our recursive TRF realization strategy can benefit the velocity  
43 estimation for campaign stations.

44 **Keywords:** Recursive TRF realization, TRF-related system errors, CMONOC, RMS

45

## 46 **Introduction**

47 With the development of Global Positioning System (GPS) technology and the  
48 rapid accumulation of GPS stations and observations, GPS geodesy has contributed to  
49 significant advances and been widely employed in tectonics, geophysics, seismology,  
50 atmosphere science, and hydrology (Bock and Melgar 2016). Since 1998, China  
51 Earthquake Administration has launched the national scientific project, namely the  
52 Crustal Movement Observation Network of China (CMONOC), to monitor the spatial-  
53 temporal characteristics of crustal deformation in China mainland and surrounding  
54 areas (Wang et al. 2001). In the CMONOC, dozens of continuous GPS stations have  
55 accumulated 22 years of observations, and several hundreds of stations have been  
56 operated for more than 10 years incessantly (Zheng et al. 2017). In the view of  
57 geodesists, the crucial and urgent scientific issues are concentrated on the refinement  
58 of estimation strategies of GPS stations’ coordinates, as well as the elimination of errors  
59 in the coordinate time series (Bock et al. 2000).

60 For the high-precision estimation of GPS stations' coordinates, Bernese is one the  
61 most widely used software (Dach et al. 2015), which provides considerable thorough  
62 supports and services, regular updates and has rapid growth of user communities,  
63 including the GEONET (Global Navigation Satellite System Earth Observation  
64 Network System) (Sagiya 2004), the EPN (Europe Permanent Network) (Kenyeres and  
65 Bruyninx 2004) and the CMONOC (Wu et al. 2018). As regards to the processing  
66 strategies on the Bernese platform, the EPN center and the Center of Orbit  
67 Determination in Europe (CODE) have proposed conventional recommendations for its  
68 application on regional geodetic network (Dach et al. 2009). The critical points on the  
69 formation of coordinate normal equations (NEQs) are to keep the positions of satellites'  
70 orbits and the Earth rotation parameters (ERPs) fixed to their nominal values, which  
71 are inherited from official International GPS Service (IGS) or CODE products (Dach  
72 et al. 2009). Kotsakis and Chatzinikos (2017) pointed out that the derived coordinate  
73 NEQs would contain redundant and weak frame-origin-related terrestrial reference  
74 frame (TRF) contents, thus inducing rank deficient problems and network distortions  
75 in the coordinate estimation from NEQs. Kotsakis and Chatzinikos (2017) proposed the  
76 so-called controlled datum removal (CDR) filter to solve the intrinsic defects in Bernese  
77 processing. With the CDR filter, they reconstructed the NEQs with the geometric  
78 information of geodetic network fully retained and redundant TRF contents abandoned,  
79 thus conforming to the requirement of necessary rank deficiencies in the employment  
80 of the minimum constraint for the least squares estimation of stations' coordinates  
81 (Rebischung et al. 2014). Wu et al. (2018) augmented the CDR algorithm on the  
82 filtering of other redundant TRF contents from NEQs, and suggested to solely remove  
83 the weak frame-origin-related contents in the processing of regional geodetic network.

84 By means of the application of minimal constraints on the NEQs, the  
85 underdetermined coordinates of GPS stations get constrained and estimable by a set of  
86 fiducial stations with their coordinates being nominally known, yielding the TRF  
87 realization of stations' coordinates (Altamimi et al. 2016). Conventionally, the nominal  
88 coordinates of fiducial stations are interpolated or extrapolated by their trajectory  
89 models defined in specific TRF, such as ITRF2014. As a general model, the ITRF2014

90 trajectory model lacks seasonal modeling parameters, and degrades to piece-wise linear  
91 modeling of some nonlinear signals occasionally, thus yielding insufficient accuracy of  
92 the nominal coordinates for the fiducial stations (Altamimi et al. 2016). Due to the  
93 insufficient modeling problem, some researchers had identified centimeter-level  
94 seasonal oscillations on the up component of GPS coordinate time series, which biased  
95 their “real” values and corresponding physical interpretations significantly (Zou et al.  
96 2014). As a hysteretic system, ITRF2014 was established by historic geodetic data  
97 before 2014 (Rebischung et al. 2016). The subsequent incidents (e.g., earthquakes and  
98 GPS antenna changes) will bias the trajectory models and lead the so-called TRF  
99 realization errors into the extrapolated nominal coordinates. Due to these innate flaws  
100 in the ITRF2014 trajectory models, the total number of fiducial stations varies  
101 temporally, thus inducing temporal instability for the fiducial network and leading  
102 system errors into the estimated coordinate time series. Furthermore, the imperfect and  
103 globally uneven spatial distribution of fiducial network can generate the so-called  
104 network effects and bias the results of TRF realization (Collilieux et al. 2011). Legrand  
105 et al. (2012) had found that the network effects could bias the estimation of EPN stations’  
106 coordinates up to 6 ~ 10 mm, as well as the estimated secular trends from coordinate  
107 time series up to 1 ~ 3 mm/year. We summarize these propagated errors stemmed from  
108 TRF defects as TRF-related system errors. To overcome the limitation of conventional  
109 TRF realization and mitigate TRF-related system errors, Bevis and Brown (2014)  
110 proposed a comprehensive trajectory model and employed a recursive TRF realization  
111 strategy in the processing of global GPS network, obtaining considerable root mean  
112 squares (RMS) reduction and significant improvements of accuracies for the estimated  
113 coordinate time series.

114 In this paper, we elaborate the practical strategy on the eliminating of TRF-related  
115 system errors in the coordinate time series for the CMONOC GPS stations. In section  
116 2, we briefly introduce the CMONOC GPS data set and present conventional models  
117 used in the Bernese processing as well as the rank defect analysis of NEQs. In section  
118 3, we present the details of both conventional and recursive TRF realization strategies.  
119 In section 4, we present the results from both TRF realizations and the comparisons

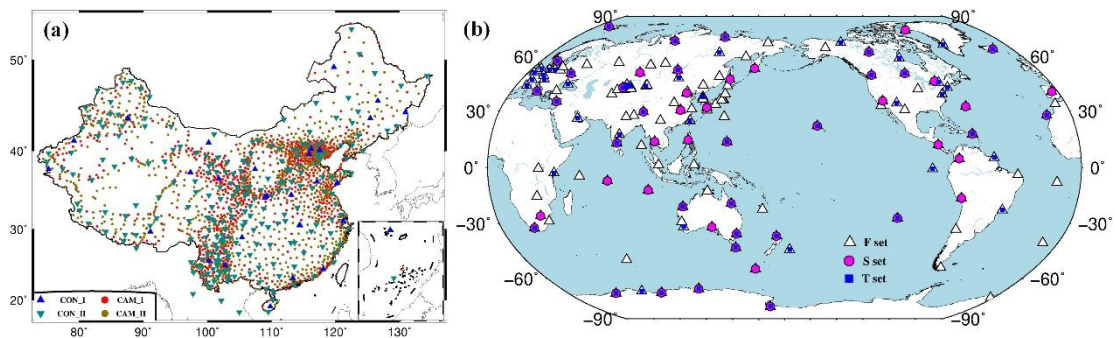
120 between the derived RMS for coordinate time series. In section 5, we present the  
121 comparisons between our recursive TRF realization strategy with Bevis and Brown  
122 (2014), as well as two noise filters, and reveal the essence of our recursive TRF  
123 realization strategy. In section 6, we give the conclusion of this paper.

124

## 125 **GPS data and processing**

### 126 **GPS data set**

127 We have included all the CMONOC (Figure 1a) GPS data in the daily processing.  
128 To the deadline of this study, 27 (CON\_I) continuous stations have a long time-  
129 occupation history from 1998 to the end of 2019, with the time span being about 22  
130 years; while the remaining 260 (CON\_II) continuous stations have been installed and  
131 operated since later 2010, with the data volume being about 10 years. In addition, we  
132 simultaneously include campaign stations in the geodetic network, with the total  
133 number being 1083 for CAM\_I and 1074 for CAM\_II, respectively (Wang and Shen  
134 2020). To implement the conventional TRF realization of daily coordinates, we also  
135 include 152 (F set) globally distributed ITRF stations (Figure 1b), which are candidates  
136 of the ITRF2014 fiducial stations (Rebischung et al. 2016).



137

138 Figure 1. The spatial distribution of our geodetic network. (a) is the spatial distribution  
139 of the CMONOC, with blue triangles being CON\_I continuous stations, dark cyan  
140 invert triangles being CON\_II continuous stations, red circles being CAM\_I campaign  
141 stations and dark gold circles being CAM\_II campaign stations, respectively; (b) is the  
142 spatial distribution of ITRF fiducial stations, with F set being the full set, S set being  
143 the stable set, and T set being the transformations set, respectively .

144

## 145 **Daily processing**

146 The whole GPS data set are routinely processed for daily coordinate NEQs by the  
147 Bernese 5.2 software. The conventional Bernese processing strategy is adopted from  
148 EPN and CODE (Bruyninx et al. 2012), with general models recommended by the  
149 International Earth Rotation Service (Petit et al. 2013). In addition, FES2004 ocean  
150 tidal loading corrections (Lyard et al. 2006), atmospheric S1-S2 tidal loading  
151 corrections (Tregoning and Watson 2009) and absolute phase-center corrections  
152 (Schmid et al. 2015) for both satellites and receivers are applied on the formulation of  
153 the observation equations of GPS data. The tropospheric delay is modeled by using the  
154 Vienna Mapping Function (VMF), with zenith delay hourly estimated for the wet-part  
155 and VMF model values assigned for the dry-part (Landskron and Böhm 2018). First-  
156 order ionospheric delays are eliminated by means of the ionosphere-free linear  
157 combination of GPS observations, and higher-order terms are modeled as  
158 recommended in Petrie et al. (2010). Satellites orbits and the ERPs are introduced from  
159 reprocessed (1999-2015) and regular (2015-2019) CODE products, respectively, to  
160 assure the consistency of TRF in the daily solution (Wu et al. 2018). Meanwhile, they  
161 are recommended to be retained fixed in the final least squares estimation of the  
162 position parameters, together with phase ambiguities resolved as much as possible and  
163 geometrical correlations among GPS stations fully considered (Dach et al. 2009). With  
164 nuisance parameters (e.g., tropospheric coefficients and ambiguities) eliminated from  
165 the final NEQ, we obtain the reduced daily coordinate NEQ, which is given in the  
166 linearized form as:

$$167 \quad N(X - X_0) = u \quad (1)$$

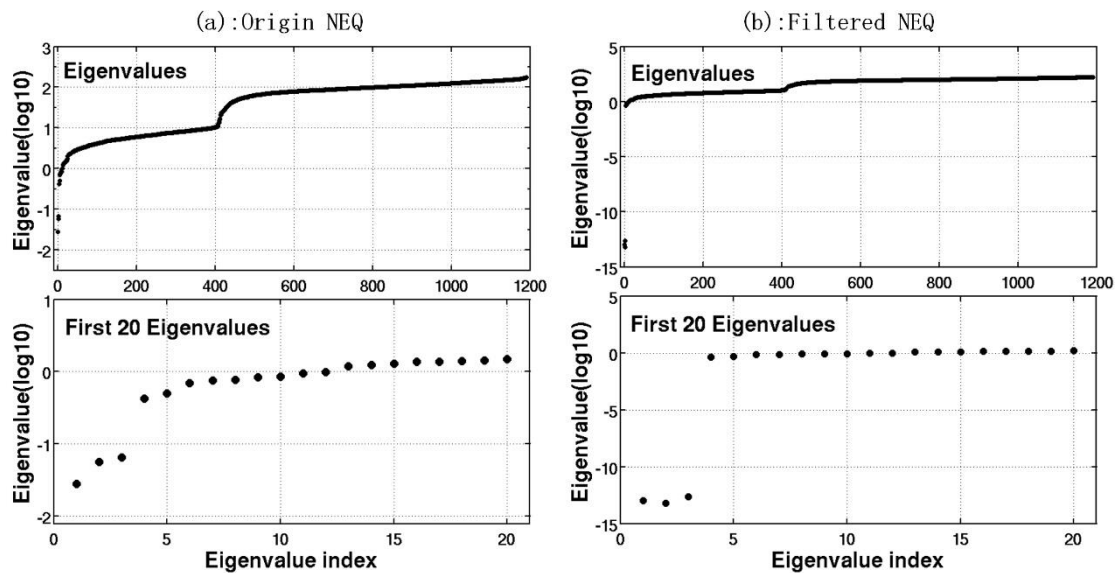
168 where  $N$  is the coordinate NEQ,  $X$  is the vector of estimated GPS station position  
169 parameters,  $X_0$  is the vector of the a priori coordinates, and  $u$  is the right-hand side  
170 normal vector, respectively.

171

## 172 **Rank defect analysis and TRF stripping**

173 Following the suggestion from Wu et al. (2018) on the processing of CMONOC

174 GPS data, we sequentially reprocess all daily NEQs. As an example, we present the  
 175 eigenvalue properties of two coordinate NEQs on the day 101 of 2014, the original one  
 176 and the filtered one with frame-origin-related TRF contents fully removed, respectively.  
 177 As shown in Figure 2a, the smallest eigenvalues range from  $10^{-2}$  to  $10^{-1}$ , which largely  
 178 reflect the weak frame-origin-related contents in the NEQ; the condition number of the  
 179 matrix (the ratio between the maximum and minimal eigenvalues) is about  $10^4$ , thus  
 180 implying a rather well-conditioned invertible matrix without any real rank deficiency  
 181 for the original NEQ. While in the Figure 2b, we can see that the filtered NEQ matrix  
 182 has 3 rank deficiencies, with the three smallest eigenvalues being in the order of  $10^{-13}$ ,  
 183 and having an apparent gap of  $10^{12}$  relative to the rest eigenvalues. We can conclude  
 184 that the CDR filter recovered the rank deficient property of the NEQ matrix, which is  
 185 explicitly needed in the least squares estimation of GPS station coordinates.  
 186 Furthermore, both the complete geometric information of GPS networks and frame-  
 187 orientation/scale-related contents are fully retained in the NEQ matrix (Wu et al. 2018),  
 188 which reflected the superiority of the CDR algorithm on the filtering of redundant TRF  
 189 contents from NEQs.



190  
 191 Figure 2. Eigenvalue property of the NEQ matrix on the 2014101. (a) is for the original  
 192 NEQ matrix; (b) is for the frame-origin-related TRF contents filtered NEQ matrix,  
 193 respectively.

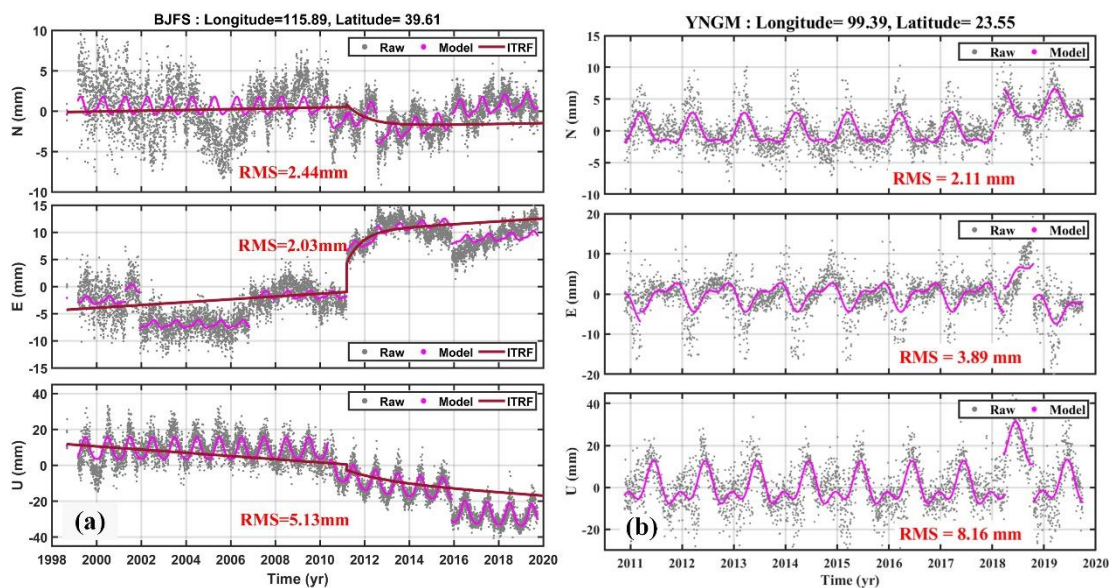
194

195 **TRF realization strategies**

196 **Conventional strategy**

197 By following the ITRF convention, the daily TRF realization of stations'  
198 coordinates is operated through a set of fiducial stations, via the alignment of their  
199 estimated coordinated to their nominal coordinates (interpolated or extrapolated from  
200 ITRF2014 trajectory models) with a Helmert transformation (Altamimi et al. 2016). As  
201 described in previous section, the filtered daily NEQs have 3 rank deficiencies, and  
202 retain the frame-orientation/scale-related contents inherited from satellite ephemeris,  
203 thus requesting the supplement of the frame-origin-related information from the 3-  
204 parameters Helmert transformation.

205 As shown in Figure 1b, we have included 152 ITRF2014 fiducial stations (F set)  
206 in our geodetic network, which were globally unevenly distributed. To mitigate the so-  
207 called network effect (Collilieux et al. 2012), we pick out 70 stations to form a new  
208 fiducial set, the stable set (S set). These 70 stations are selected with steady temporal  
209 behaviors, good continuity qualities and homogeneous and symmetry distribution on  
210 the Earth surface to the maximum extent. According to Wu et al. (2018), the S set  
211 fiducial network is superior to the F set or a regional one, due to its mitigating feature  
212 on the network effect. Therefore, the S set fiducial network is applied to realizing the  
213 ITRF2014 for the estimation of station positions.



214

215 Figure 3. Detrended coordinate time series. (a) is for the CON\_I and ITRF fiducial

216 station BJFS, (b) is for the CON\_II station YNGM. To view the time series, we subtract  
217 the secular trend signals from all three components, with the gray dots representing raw  
218 data, magenta dots representing the integral trajectory models employed in this study  
219 and brown lines representing ITRF2014 trajectory models.

220

221 The time evolution of trajectory models for fiducial stations are adopted from  
222 Altamimi et al. (2016) in their construction of the ITRF2014. The trajectory model not  
223 only includes general linear models but also non-linear model to simulate post-seismic  
224 effects of great earthquakes. Implementing with the S set fiducial network and the ITRF  
225 trajectory models, we perform TRF realization on the basis of daily coordinate NEQs,  
226 forming the nominal coordinate time series under the ITRF2014.

227

## 228 **Recursive strategy**

229 The recursive strategy is inspired from the processing strategy for global network,  
230 referring to Bevis and Brown (2014). As their iterative methods were employed on the  
231 basis of GAMIT/GLOBCK results, we adapt it to the Bernese results and apply to the  
232 processing of CMONOC data. We can split the workflow into three steps:

### 233 (1) Time series modeling

234 The principle of time series modeling is to best fit the coordinate time series,  
235 despite of possible cross-coupling between linear and non-linear model parameters.  
236 Towards coordinate time series containing significant post-seismic signals (Tobita  
237 2016), Bevis and Brown (2014) pointed out that the set of non-linear models as well as  
238 diverse decay coefficients in the modeling of post-seismic signals had negligible  
239 impacts on the effectiveness of time series fitting, indicating that we can set an uniform  
240 logarithm function with decay time being 1 year for all stations and components. In  
241 addition, both annual and semi-annual functions should be included to handle seasonal  
242 signals conventionally. Therefore, our integral trajectory model can be described as:

$$\begin{aligned} \overset{v}{X}(t) = & \overset{v}{X}_R + \overset{v}{V}(t-t_R) + \sum_{j=1}^{n_j} \overset{v}{b}_j H(t-t_j) + \sum_{m=1}^{n_M} \overset{v}{v}_m (t-t_m) H(t-t_m) \\ & + \sum_{k=1}^{n_p} [\overset{v}{s}_k \sin(\omega_k t) + \overset{v}{c}_k \cos(\omega_k t)] + \sum_{i=1}^{n_L} \overset{v}{A}_i^L \log(1+t-t_i^L) H(t-t_i^L) \end{aligned} \quad (2)$$

243

244

245 where  $t$  is the target epoch,  $t_R$  is the reference epoch,  $\overset{v}{X}(t)$  is the estimated  
 246 position,  $\overset{v}{X}_R$  is the reference position,  $\overset{v}{V}$  is the station velocity,  $n_j$ ,  $n_M$  and  $n_L$   
 247 are the total number of offsets, velocity changes and logarithmic functions models,  
 248 respectively,  $t_j$ ,  $t_m$  and  $t_i^L$  are corresponding model epochs,  $H(t-t_j)$ ,  
 249  $H(t-t_m)$  and  $H(t-t_i^L)$  are corresponding Heaviside functions,  $\overset{v}{b}_j$ ,  $\overset{v}{v}_m$  and  $\overset{v}{A}_i^L$   
 250 are corresponding coefficients,  $\tau_i^L$  is the relaxation time for the non-linear function  
 251 models, respectively.  $n_p$ ,  $\bar{s}_k$  and  $\bar{c}_k$  are coefficients of periodic functions,  $\omega_k$  is  
 252 the corresponding frequency. Note that the number of “velocity changes”, “offsets” and  
 253 possible “post-seismic” signals are identified with auto-detection module by the  
 254 Bernese 5.2 software with artificial confirmation (Dach et al. 2009). Hundreds of offsets  
 255 and logarithm functions are set and verified for CMONOC stations due to the 2011.3.11  
 256 Tohoku earthquake (Nishimura et al. 2011).

257 As seen in Figure 3, not only the prominent seasonal signals but also some subtle  
 258 offsets, such as the two satellite orbits-related offsets on the 2001308 and 2006335 (Wu  
 259 et al. 2018) for BJFS (Figure 3a), are taken into account in our integral trajectory model.  
 260 Furthermore, the outstanding offset for BJFS in the end of 2015 is identified and  
 261 considered, while it is ignored in the ITRF2014 trajectory model due to its lag to the  
 262 establishment of the ITRF2014. The full set of formed coordinate time series are  
 263 modeled with equation (2). A set of trajectory model parameters and corresponding root  
 264 mean square (RMS) of residual time series are obtained.

265 (2) TRF realization

266 Nearly the full set of continuous stations is assigned as “pseudo” fiducial stations,  
 267 with the selection criterion being as: data occupation > 2.5 years and data efficiency >

268 70%. Based on the new definition, the TRF realization is re-performed. Then, another  
269 loop of time series modeling is applied to obtain a new set of model parameters and  
270 corresponding RMS results for coordinate time series.

271 The iterative campaign is triggered through the salience of RMS reduction  
272 between current and previous loops, where the criterion is set to 1% on average. As the  
273 iterative campaign stop, we obtain the final coordinate time series and trajectory model  
274 parameters.

### 275 (3) Frame alignment

276 The secular parameters and initial positions of well-behaved ITRF2014 stations  
277 are picked out to form a Helmert transformation between the derived and nominal ones,  
278 with corresponding transformation coefficients employed to implement the alignment  
279 of the final coordinate time series to the ITRF2014 reference frame (Bevis and Brown  
280 2014).

281

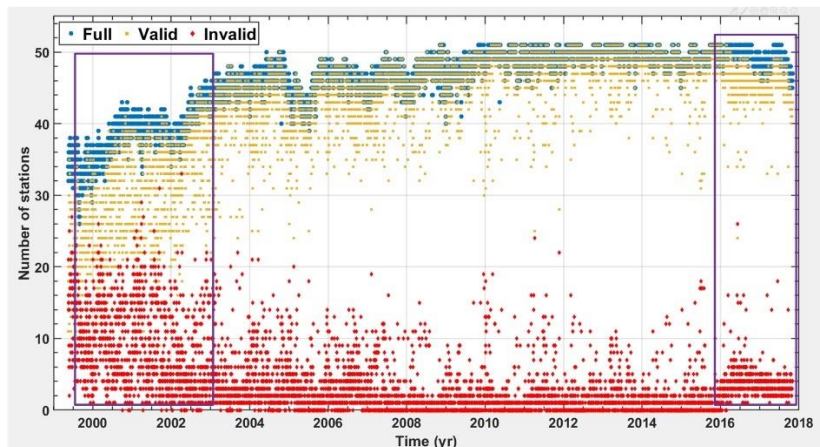
## 282 **Results**

### 283 **Conventional TRF realization**

284 During the TRF realization, the nominal coordinates of fiducial stations are  
285 modeled with ITRF2014 trajectory models, and a necessary Helmert validation  
286 algorithm is utilized to verify the validity of fiducial stations, which is an index to  
287 qualify the accuracy of the nominal coordinates. The more the number of valid fiducial  
288 stations are, the more precise the nominal coordinates. By convention, the thresholds  
289 are set to 10 mm and 30 mm between the nominal and the estimated coordinates for  
290 horizontal and vertical components, respectively (Dach et al. 2015).

291 In Figure 4, we present the statistic of full, valid and invalid set of fiducial stations  
292 employed in the daily TRF realization, respectively. As we have shown in Figure 1b,  
293 the total number of stations in the S set fiducial network is 70, while it is less than 51  
294 daily. The total number of valid/invalid stations is quite scattered in the period,  
295 indicating temporal instability of daily TRF realization. At both sides of the interval,  
296 the total number of valid stations both get shrinking, indicating more failures on the  
297 interpolating/extrapolating of the nominal coordinates from the ITRF2014 trajectory

298 models. The phenomenon can be associated with the innate flaw of the short-term  
299 availability for the ITRF2014 trajectory models. As the ITRF2014 trajectory models  
300 are well estimated with data before 2014, the discrepancies between the model and “real”  
301 values gradually increase over time due to some incidents, such as earthquake events  
302 and equipment changes (e.g., in Figure 3a). Therefore, we cannot hold the fiducial  
303 network stable in both temporal and spatial domain, thus bringing TRF-related  
304 systematic errors into the estimated coordinate time series.



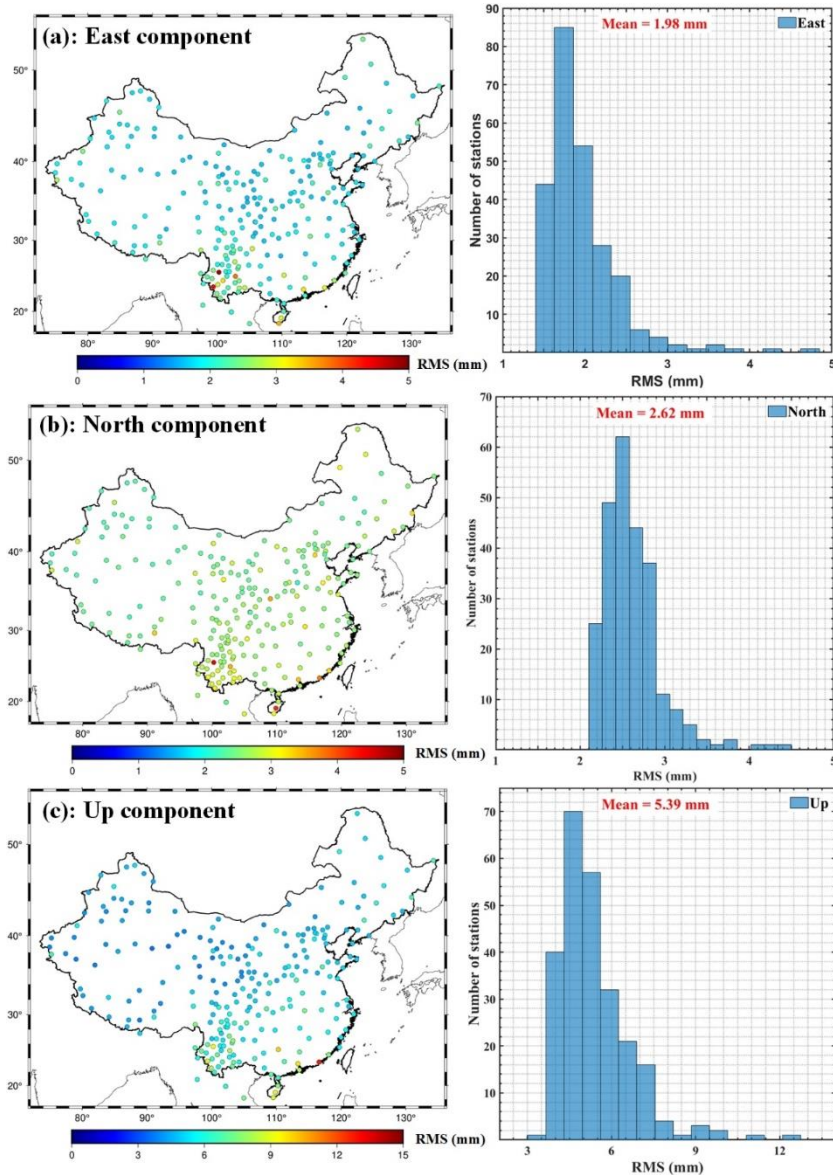
305

306 Figure 4. Statistic of the total number of fiducial stations in the conventional TRF  
307 realization of coordinates. The purple rectangles outline the shrinking periods.

308

309 **Recursive TRF realization**

310 **Time series modeling**



311

312 Figure 5. Statistic of RMS of raw coordinate time series for CMONOC GPS stations.

313 (a) - (c) are for the east, north and up components, respectively. The left figures are

314 spatial distributions and the right figures are histograms of the RMS respectively.

315

316 With best-fitting performed on continuous coordinate time series, we obtain their

317 residuals and corresponding RMS. For the CMONOC continuous stations, the average

318 RMS is 1.98mm, 2.62 mm and 5.39 mm for east, north and up components, respectively

319 (Figure 5). The RMS on the up components are 2 ~ 3 times larger than the horizontal

320 ones, indicating the relative precision between horizontal and vertical components from

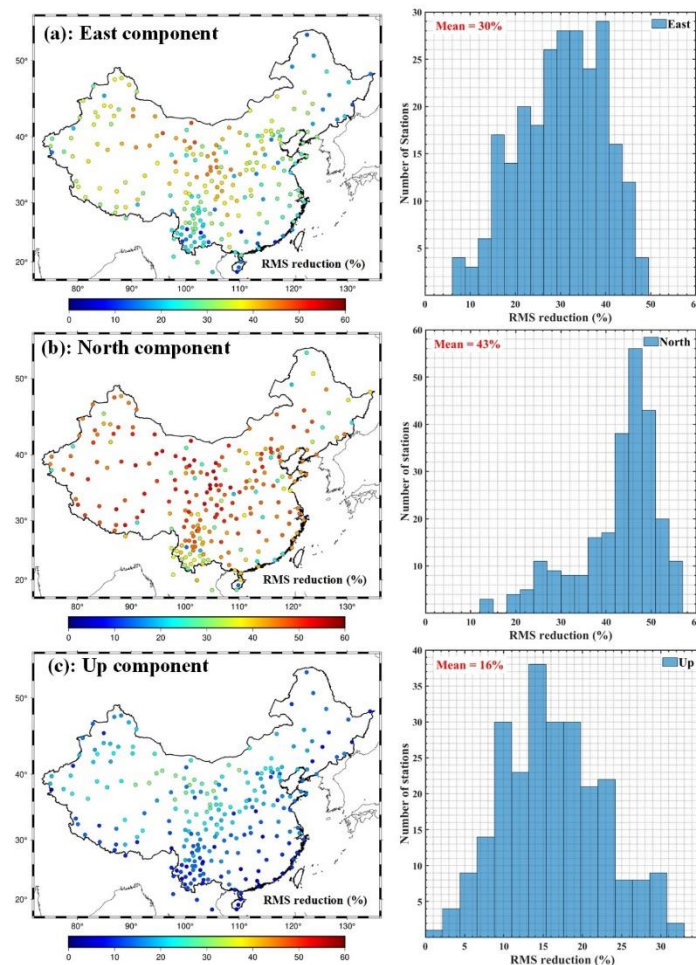
321 GPS positioning. The north components have larger RMS than the east components,

322 which could origin from the asymmetrical distribution of fiducial network in the  
 323 northern and southern hemispheres of the Earth. In total, the RMS of CMONOC  
 324 stations in southern part have larger quantities than in the northern part, partially  
 325 because of the noisy environment in the rainy and woody southern district, especially  
 326 in the Yunnan province, southeastern part of China (Zhan et al. 2017), where the station  
 327 holds abnormal jitters annually in the winter season from November to February (e.g.,  
 328 the station YNGM in Figure 3b).

329

### 330 TRF realization

331 The whole set of continuous stations are treated as “pseudo” fiducial network, with  
 332 nominal coordinates equaling with the model values derived from the time series  
 333 modeling. We employ the first loop of TRF realization, and obtain a new set of  
 334 coordinate time series, with fresh RMS results following the time series modeling.



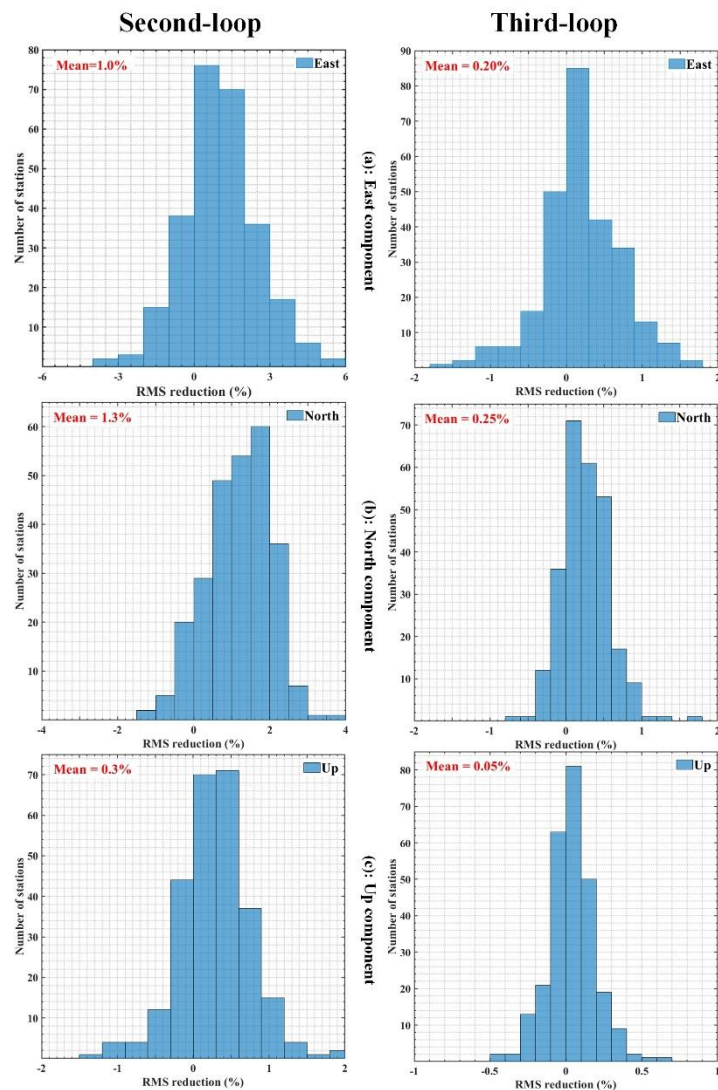
335

336 Figure 6. Statistic of the percentage of RMS reduction in the first-loop for CMONOC

337 coordinate time series. (a) - (c) are respectively. The left figures are spatial distribution  
 338 and the right figures are histograms of RMS reduction respectively.

339

340 The whole set of CMONOC stations get significant RMS reduction in all three  
 341 components, whereas the extracted secular trends, periodic signals have negligible  
 342 differences. As shown in Figure 6, the average percentage of RMS reductions are 30%,  
 343 43% and 16% in the east, north and up components, respectively. The significance of  
 344 RMS reduction in the north component is the most remarkable, whereas the up direction  
 345 holds the lowest percentage of RMS reduction on the contrary. Compared to the spatial  
 346 distribution of RMS in Figure 5, the spatial distribution of the percentage of RMS  
 347 reduction has identical pattern, with CMONOC GPS stations in the southern part having  
 348 lower values.

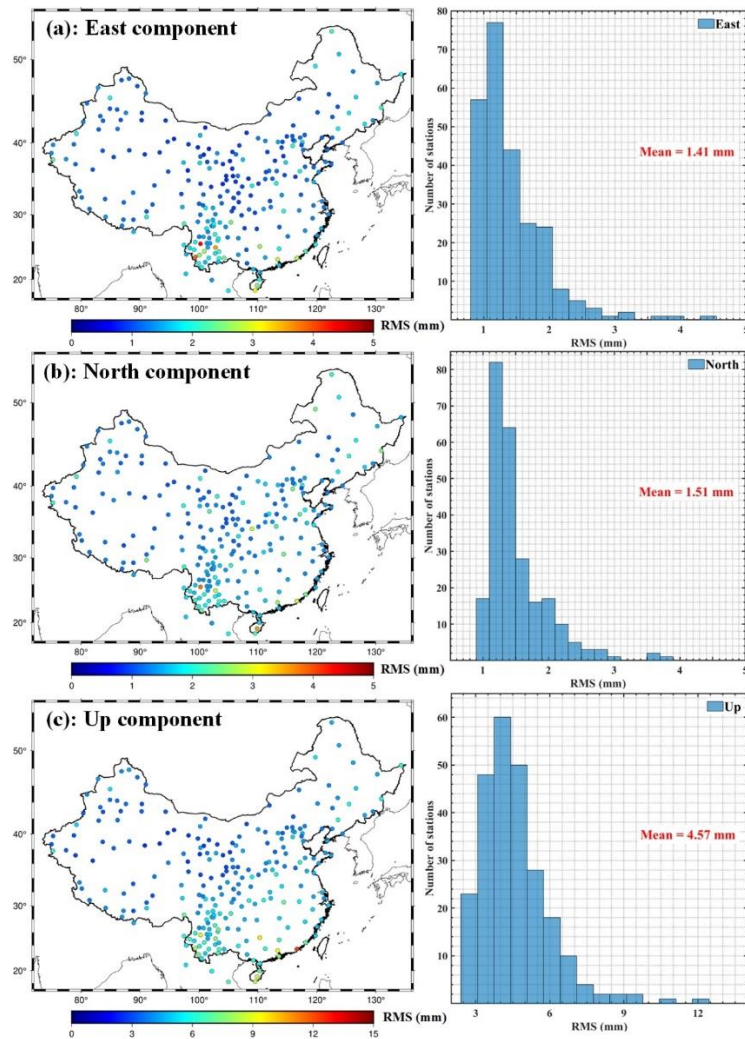


349

350 Figure 7. Statistic of the percentage of RMS reduction in the second- and third-loops  
351 for CMONOC coordinate time series. (a) - (c) are for the east, north and up components,  
352 respectively. The left figures are for the second-loop and right figures are for the third-  
353 loop.

354

355 In the second loop, we repeat the same operations with initial nominal coordinates  
356 derived from time series modeling of coordinates time series for the first loop. At this  
357 time, the RMS reductions rapidly drop to less than 10% for all stations in all  
358 components, with the mean values being 1.0%, 1.3% and 0.3% for the east, north and  
359 up components, respectively, and the maximum reduction being 4 - 6% and < 2% in  
360 horizontal and vertical directions, respectively. Note that some stations present RMS  
361 amplification up to 1%-4% in the CMONOC. In the third loop, the percentages of RMS  
362 reduction tend to be negligible, with the mean values being 0.20%, 0.25% and 0.05%  
363 for the east, north and up components, respectively, and the maximum values being less  
364 than 2%.



365

366 Figure 8. Statistic of RMS of the final coordinate time series for CMONOC GPS  
 367 stations. (a) - (c) are for the east, north and up components, respectively. The left figures  
 368 are spatial distributions and the right figures are histograms of the RMS respectively.

369

370 Finally, we terminate the iterations of TRF realization at the end of the third loop,  
 371 and regard the derived coordinate time series as the final results. As shown in Figure 8,  
 372 the mean RMS for the new set of coordinate time series are 1.41 mm, 1.51 mm and 4.57  
 373 mm in the east, north and up components, respectively. The vertical RMS is nearly 3  
 374 times to the horizontal ones. In total, the stations in the central part of CMONOC have  
 375 the minimal RMS quantities, whereas in the outer areas, especially the southeastern part,  
 376 RMS values are higher in all three components. The average RMS values are nearly  
 377 equal for both horizontal components, indicating that the recursive TRF realization  
 378 could eliminate the kind of system errors which are related to the defective distribution

379 of the fiducial network.

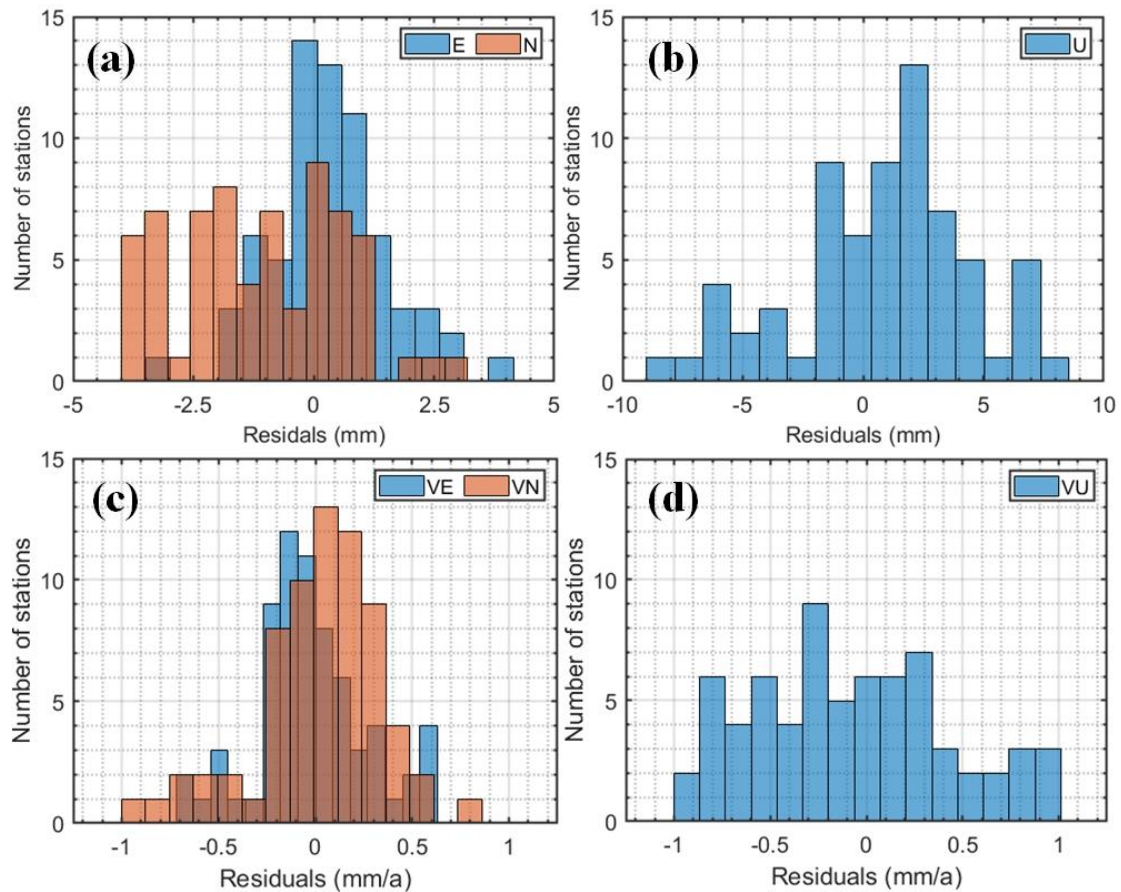
380

### 381 **Frame alignment**

382 Because our recursive TRF realization does not follow the standard ITRF  
383 conventions, the reference frame of the final coordinate time series would not be  
384 consistent with the ITRF2014 exactly. As the differences are minor, a linear similarity  
385 transformation could be employed to align the final frame to the ITRF2014.

386 Among the included 152 ITRF2014 fiducial stations, we pick out 68 stations  
387 (Figure 1b), namely the transformation set (T set), which meet five strict criteria: the  
388 time occupation should be longer than 10 years; the degree of completeness of time  
389 series should be larger than 80%; there are no significant changes on the secular trends;  
390 there are no significant non-linear signals; the RMS values should be less than 5 mm  
391 and 10 mm in the horizontal and vertical components, respectively. Most of the T set  
392 stations are located in the middle Asia, Europe, north America, Australia and Antarctica,  
393 where few great earthquakes occur.

394 During the recursive TRF realization, only the frame-origin related parameters of  
395 reference frame are daily set through the 3-parameters Helmert transformation, whereas  
396 the frame-orientation and scale-related parameters are kept and inherited from the  
397 satellite orbits. Therefore, to realize the frame alignment between our recursively  
398 defined TRF and the standard ITRF2014, we should only consider their origin-related  
399 differences, indicating that only the 6-parameters (3 for the origin and 3 for the time  
400 evolution of the origin) Helmert transformation should be employed in the alignment.



401

402 Figure 9. Residuals of the Helmert transformation between the recursively defined TRF  
 403 and the ITRF2014. (a) and (b) are residuals of station coordinates at epoch 2010.01.01  
 404 for horizontal and vertical directions, respectively, (c) and (d) are residuals of station  
 405 velocities for horizontal and vertical directions, respectively.

406

407 Through the Helmert transformation with 68 ITRF2014 fiducial stations, the  
 408 estimated origin shift parameters are 0.50 mm, 0.16 mm and 0.71 mm, respectively, as  
 409 well as the origin shift rate being 0.04 mm/a, 0.09 mm/a and -0.09 mm/a, respectively.  
 410 We present the residuals of the Helmert transformation in Figure 9. The coordinate  
 411 residuals are in the interval of (-5, 5) mm and (-10, 10) mm, with WRMS being 1.23  
 412 mm, 1.73 mm and 3.67 mm for horizontal and vertical components, respectively, and  
 413 the velocity residuals are in the interval of (-1, 1) mm/a, with WRMS being 0.29  
 414 mm/year, 0.33 mm/year and 0.51 mm/year for horizontal and vertical components,  
 415 respectively. The quantities of transformation parameters (less than 1 mm and 0.1 mm/a)  
 416 are negligible, thus indicating that our recursively defined TRF is similar with the

417 ITRF2014. In the end, we apply the 6-parameters Helmert transformation to the  
418 remaining stations with the same transformation parameters, yielding the final  
419 coordinate time series in the ITRF2014.

420

## 421 **Discussion**

### 422 **Comparison with Bevis and Brown (2014)**

423 The recursive TRF realization strategy is inspired from the processing of global  
424 GPS data in the Ohio State University, which is handled by the GAMIT/GLOBK  
425 software (Bevis and Brown 2014). They constructed a set of trajectory models (namely  
426 Standard Linear Trend Model) to fit the coordinate time series to the maximum extent,  
427 and refined the parameters of the trajectory model from iterative reprocessing of  
428 stations' coordinates and satellites' orbits simultaneously. Their results showed a  
429 significant RMS reduction in the coordinate time series, to 2.3 mm and 4.7 mm in the  
430 horizontal and vertical components, respectively, which reached a >50% RMS  
431 reduction overall. The RMS derived from the alignment between their final TRF and  
432 the ITRF2008, were 5.3 ~ 8.2 mm and 0.55 ~ 0.64 mm/year for coordinates and  
433 velocities in the X, Y and Z directions respectively.

434 As our CMONOC network is centralized in China, the regional spatial distribution  
435 limits the capacity of simultaneous estimation of stations' coordinates, satellite orbits  
436 and ERPs, thus reducing the degree of freedom to only 3 translation parameters for the  
437 realization of the inner geometry into the target TRF. These intrinsic deficits weaken  
438 the quantities of RMS reduction to only 16% ~ 43% averagely in our data set, by letting  
439 the system errors inherited from satellite sites propagate into stations' coordinates.

440 Overall, our strategy is suit for regional GPS data processing, whereas Bevis and  
441 Brown's (2014) original procedures are more practical for the handling of global  
442 geodetic network.

443

### 444 **Comparison with regional filtering strategies**

445 In general, the primary effect of our recursive TRF-realization is identical to a  
446 noise filter Compared to some of the general noise filtering methods, such as stacking

447 (Tian and Shen 2016) and principle component analysis (PCA) (Dong et al. 2006), there  
448 are mainly 3 distinct aspects:

449 (1) Both stacking and PCA methods are directly employed on the coordinate level, with  
450 the so-called “common mode errors (CMEs)” explicitly extracted and deducted  
451 from the coordinate time series. While our recursive strategy is handled on the NEQ  
452 level, ahead of the derivation of coordinate solution, with system errors implicitly  
453 reduced in the TRF realization.

454 (2) Both stacking and PCA methods are practical in a limited (regional) area, where the  
455 demand of “uniformity”, either similar deformation pattern for stacking  
456 (Wdowinski et al. 1997) or uniform spatial response for PCA (Dong et al. 2006), can  
457 be met. While no “uniformity” of spatial response is required in our recursive  
458 strategy, indicating no limitation on the spatial distribution of processed geodetic  
459 network.

460 (3) The CMEs extracted by stacking and PCA methods are statistically defined, with  
461 no explicit physical meanings, comprising of large-scale system errors, medium-  
462 scale environmental errors or signals, as well as considerable local effects. While  
463 our recursive strategy precisely aims at the specific TRF-related system errors.

464 Therefore, our recursive strategy is quite efficient and effective on the filtering of  
465 TRF-related system errors regardless of the limitation of the scope of geodetic network,  
466 which is primarily taken into account for other noise filters.

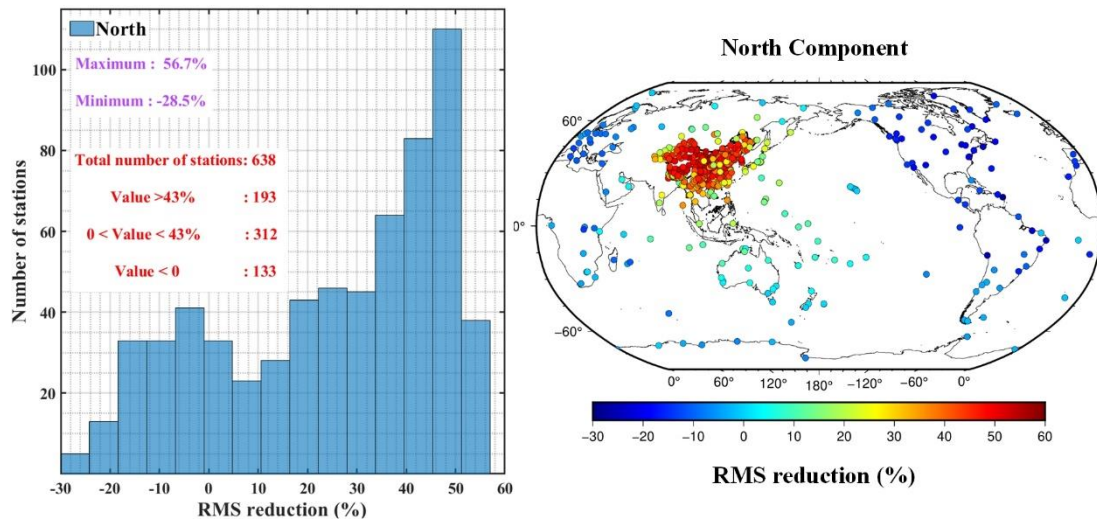
467

#### 468 **The essence of recursive TRF realization**

469 The incompleteness of ITRF trajectory models, such as mismodeling and under-  
470 modeling, as well as the uneven distribution of fiducial network (the so-called “network  
471 effects”), would lead to signal leakage from fiducial stations to undetermined stations,  
472 which can be defined as TRF-related system errors (Bevis and Brown 2014). Moreover,  
473 the misfits between “real” and interpolated/extrapolated nominal coordinates for  
474 fiducial stations also introduce significant errors into the estimation of coordinates.

475 The essential benefit of our recursive strategy is to eliminate TRF-related system  
476 errors in the coordinate time series. As nearly the whole set of stations are properly

477 fitted with integral trajectory models, the signal leakage effects, as well as network  
 478 effects would be restrained to the maximum extent, thus suppressing the TRF-related  
 479 system errors.



480

481 Figure 10. Statistic of RMS reduction for all GPS stations in the north component. The  
 482 left figure is histogram of the percentage of RMS reduction, and the right figure is its  
 483 spatial distribution.

484

485 In Figure 10, we present the statistic of RMS reduction for all stations in the north  
 486 component. We find that 193 stations, located in the center of the CMONOC, get  
 487 significant RMS reduction, with the value being larger than the average quantity of 43%,  
 488 up to 56.7%; 312 stations, mostly in and around the CMONOC, have RMS reductions  
 489 between 0 and 43%, indicating positive improvement on the accuracy of coordinate  
 490 time series; the remaining 133 globally distributed stations hold negative RMS  
 491 reduction, down to -28.5%. To understand this pattern, we should refer to the core  
 492 algorithm of TRF realization, which is the alignment of the barycenter of the target  
 493 geodetic network to their nominal point through 3 degrees of freedom of frame  
 494 translation (Wu et al. 2018). In the conventional TRF realization, the barycenter is  
 495 defined by the mean position of globally sparsely distributed ITRF2014 fiducial  
 496 stations. While in our recursive TRF realization, all stations are treated as “pseudo”  
 497 fiducial stations, and contribute to the positioning of the barycenter, thus increasing the  
 498 weight for stations in and around the dense CMONOC, as well as reducing the weight

499 of other stations on the contrary, in the least squares adjustment. The more weight  
500 indicates tighter constraints imposed on the estimation of coordinates, resulting in  
501 compact coordinate time series, as well as minor RMS accordingly. Although the outer  
502 stations get slight RMS amplification, the integral trajectory model enhances the fitting  
503 accuracy of coordinate time series, thus eliminating alias effects among derived signals.

504 By inspecting the RMS reduction of coordinate time series, we can find that the  
505 north components hold the maximum quantities, which is significant higher (43%) than  
506 other components at 30% and 16% respectively. However, the RMS are in qual for the  
507 two horizontal components. This phenomenon indicates that the conventional TRF  
508 realization underestimates the precision of coordinates time series in the north direction,  
509 which can be attributed to the extremely uneven distribution of fiducial stations in the  
510 northern and southern hemispheres of the Earth, respectively. Our recursive TRF  
511 realization reveals the “real” precision of GPS observations to  $\sim 1$  mm and  $\sim 4$  mm for  
512 horizontal and vertical components of coordinates time series, respectively. Moreover,  
513 the lowest RMS reduction in the vertical component may be attributed to the  
514 insufficient modeling of vertical coordinate time series, such as the poor resolution of  
515 unidentified offsets and non-linear signals. In the future, we will attempt to apply  
516 several signal detection algorithms to thoroughly identifying all possible offsets and  
517 non-linear signals, in order to improve the accuracy of model fitting on the vertical  
518 component of coordinate time series.

519 Through our recursive TRF realization, the RMS of coordinate time series gets  
520 remarkable reduction for the CMONOC GPS stations, thus benefiting the precision  
521 enhancement of signals extraction from coordinate time series, especially for the  
522 campaign stations, which have sparse temporal resolution.

523

## 524 **Conclusion**

525 In this study, we have processed the entire set of CMONOC GPS data from 1999  
526 to the end of 2019. Above all, we have employed the so-called CDR algorithm to  
527 remove the redundant frame translation contents from the daily NEQ, avoiding  
528 millimeter-level network distortion effects in the estimated coordinates of GPS stations.

529 To eliminate the TRF-related system errors and enhance the accuracy of coordinate time  
530 series, we have adopted the iterative TRF realization strategy, realized with 3 loops of  
531 time series modeling, TRF realization and frame alignment, obtaining remarkable RMS  
532 reduction in the final coordinate time series of CMONOC GPS stations. In our recursive  
533 TRF realization, the time series modeling with the integral trajectory model keeps the  
534 temporal stability of fiducial stations, the optimal TRF realization maintains the spatial  
535 coherence of the fiducial network, and the frame alignment guarantees the frame  
536 conformity with the ITRF2014 for the obtained coordinate time series.

537 For the conventional TRF realization, the average RMS of coordinate time series  
538 are 1.98mm, 2.62 mm and 5.39 mm for east, north and up components for the  
539 CMONOC GPS stations, respectively. With more “pseudo” fiducial stations added in  
540 the TRF realization, most CMONOC stations gets significant RMS reduction in the first  
541 loop, with the average percentage of RMS reductions being 30%, 43% and 16% in the  
542 east, north and up components, respectively. The RMS reductions drop to negligible ~  
543 1% and ~ 0.2% in the following two loops, respectively, thus resulting in the  
544 termination of loops with the mean RMS being 1.41 mm, 1.51 mm and 4.57 mm in the  
545 east, north and up components of the final coordinate time series, respectively. The  
546 frame alignment to ITRF2014 is implemented by the 6-parameters Helmert  
547 transformation with 68 well-behaved fiducial stations. The quantities of transformation  
548 parameters, less than 1 mm and 0.1 mm/a, are negligible, indicating that our recursively  
549 defined TRF is similar with ITRF2014.

550 Compared to the similar iteration strategy employed for global data processing in  
551 Bevis and Brown (2014), the regional spatial distribution of the CMONOC limits the  
552 capacity of simultaneous estimation of stations’ coordinates, satellite orbits and ERP  
553 parameters, thus reducing the degree of freedom to only 3 translation parameters in the  
554 TRF realization, and weakening the quantities of RMS reduction in our processing,  
555 implying that our strategy is feasible and limited in regional network.

556 In analogy with PCA and stacking on the elimination of errors in the coordinate  
557 time series, our recursive strategy is concentrated on the TRF-related system errors, and  
558 performed on the NEQ level with requiring no “uniformity” on the spatial response.

559 However, PCA and stacking are directly employed on the coordinate level under the  
560 demand of uniform spatial response in the regional area, with the derived CMEs from  
561 having no explicit physical meanings.

562 By inspecting the spatial pattern of the RMS reduction for the processed geodetic  
563 network, we find that the stations in the central part of the CMONOC get the most  
564 significant RMS reduction, up to 43%. On the contrary, some of the globally distributed  
565 stations, which are located on the fringe, exhibit negative RMS reduction, down to -  
566 28.5%. We interpret this spatial pattern of RMS reduction as the leaning effects of the  
567 barycenter of the processed geodetic network towards the CMONOC, inducing tighter  
568 constraints on stations in the CMONOC and looser constraints on the remaining stations  
569 during the TRF realization. The north component holds the maximum quantity of RMS  
570 reduction, which is significant higher (43%) than other components at 30% and 16%  
571 respectively. Nevertheless, the RMS quantities are in equal for both horizontal  
572 components of coordinate time series, indicating that our strategy can remedy the  
573 reference frame defects stemming from the extremely uneven distribution of fiducial  
574 network in the northern and southern hemispheres of the Earth, and retrieve the “real”  
575 precision of GPS observations to  $\sim 1.5$  mm. The low precision and lowest RMS  
576 reduction in the vertical coordinate time series, may be attributed to insufficient  
577 modeling. Our recursive TRF realization can benefit the precision enhancement of  
578 signal extraction for CMONOC stations, especially for the campaign stations.

579

## 580 **Abbreviations**

581 CDR: Controlled Datum Removal; CME: Common Mode Error; CMONOC: Crustal  
582 Movement Observation Network of China; CODE: Center of Orbit Determination in  
583 Europe; ERP: Earth rotation parameters; EPN: Europe Permanent Network; GEONET:  
584 Global Navigation Satellite System Earth Observation Network System; GPS: Global  
585 Positioning System; ITRF: International Terrestrial Reference Frame; IERS:  
586 International Earth Rotation Service; NEQ: Normal Equation; PCA: Principle  
587 Component Analysis; RMS: Root Mean Squares; TRF: Terrestrial Reference Frame;  
588 VMF: Vienna Mapping Function.

589

590 **Author's contribution**

591 Weiwei Wu and Jicang Wu conceived and designed the frame of this study; Guojie  
592 Meng guided Weiwei Wu on the implement of this study, and joined the writing of this  
593 paper; Guoqiang Zhao gave some constructive suggestions on the GPS data processing  
594 in this study. All authors read and approved the final manuscript.

595

596 **Acknowledgement**

597 The authors are grateful to the staff of the CMONOC project. The authors thank  
598 anonymous reviewers for their helpful comments and constructive suggestions. Some  
599 of the figures are created by the Generic Mapping Tools (GMT) (Wessel and Smith  
600 1991).

601

602 **Competing Interests**

603 The authors declare that they have no competing interests

604

605 **Availability of data and materials**

606 The CMONOC GPS coordinate time series in this study are available from the  
607 corresponding author upon reasonable request.

608

609 **Consent for publication**

610 Not applicable

611

612 **Ethics approval and consent to participate**

613 Not applicable

614

615 **Funding**

616 This study is supported by the National Key R&D Program of China:  
617 2019YFE0108900, the National Natural Science Foundation of China: 41874024,  
618 41674003; the Basic Research Projects of Institute of Earthquake Forecasting, China

619 Earthquake Administration: 2020IEF0710, 2020IEF0511; the Research Projects of  
620 China Seismic Experimental Site: 2018CSE0207.

621

## 622 **Author details**

623 <sup>1</sup>Key Laboratory of Earthquake Prediction, China Earthquake Administration, Beijing,  
624 100036, China. <sup>2</sup>Institute of Earthquake Forecasting, China Earthquake Administration,  
625 Beijing, 100036, China. <sup>3</sup>College of Surveying and Geo-Informatics, Tongji University,  
626 Shanghai, 200092, China.

627

## 628 **References**

- 629 Altamimi, Z., P. Rebischung, L. Métivier and X. Collilieux (2016) ITRF2014: A new release of  
630 the International Terrestrial Reference Frame modeling non-linear station motions. *J.*  
631 *Geophys Res Solid Earth* 121:6109-6131. <https://doi.org/10.1002/2016JB013098>.
- 632 Bevis, M. and A. Brown (2014) Trajectory models and reference frames for crustal motion  
633 geodesy. *J Geod* 88:283-311. <https://doi.org/10.1007/s00190-013-0685-5>.
- 634 Bock, H., G. Beutler, S. Schaer, T. Springer and M. Rothacher (2000) Processing aspects related to  
635 permanent GPS arrays. *Earth planet Sp* 52: 657-662. <https://doi.org/10.1186/BF03352259>.
- 636 Bock, Y. and D. Melgar (2016) Physical applications of GPS geodesy: a review. *Reports on*  
637 *Progress in Physics* 79(10): 106801. <https://doi.org/10.1088/0034-4885/79/10/106801>.
- 638 Bruyninx, C., H. Habrich, W. Söhne, A. Kenyeres, G. Stangl and C. Völksen (2012) Enhancement  
639 of the EUREF Permanent Network Services and Products. In: Kenyon S., Pacino M., Marti  
640 U. (eds) *Geodesy for Planet Earth. International Association of Geodesy Symposia*, vol 136.  
641 Springer, Berlin, Heidelberg. [https://doi.org/10.1007/978-3-642-20338-1\\_4](https://doi.org/10.1007/978-3-642-20338-1_4).
- 642 Collilieux, X., L. Métivier, Z. Altamimi, T. van Dam and J. Ray (2011) Quality assessment of GPS  
643 reprocessed terrestrial reference frame. *GPS Solut* 15:219-231.  
644 <https://doi.org/10.1007/s10291-010-0184-6>.
- 645 Collilieux, X., T. van Dam, J. Ray, D. Coulot, L. Métivier and Z. Altamimi (2012). Strategies to  
646 mitigate aliasing of loading signals while estimating GPS frame parameters. *J Geod* 86: 1-14.  
647 <https://doi.org/10.1007/s00190-011-0487-6>.
- 648 Dach, R., E. Brockmann, S. Schaer, G. Beutler, M. Meindl, L. Prange, H. Bock, A. Jäggi, L. Ostini  
649 (2009) GNSS processing at CODE: status report. *J Geod* 83: 353-365.  
650 <https://doi.org/10.1007/s00190-008-02181-2>.
- 651 Dach, R., S. Lutz, P. Walser, P. Fridez (Eds) (2015) *Bernese GNSS Software Version 5.2. User*  
652 *manual*, Astronomical Institute, University of Bern, Bern, Open Publishing.  
653 <https://doi.org/10.1892/boris.72297>.
- 654 Dong, D., P. Fang, Y. Bock, F. Webb, L. Prawirodirdjo, S. Kedar and P. Jamason (2006)  
655 Spatiotemporal filtering using principal component analysis and Karhunen-Loeve expansion  
656 approaches for regional GPS network analysis. *J. Geophys Res* 111: B03405.  
657 <https://doi.org/10.1029/2005JB003806>.

658 Kenyeres, A. and C. Bruyninx (2004) EPN coordinate time series monitoring for reference frame  
659 maintenance. *GPS Solutions* 8: 200-209. <https://doi.org/10.1007/s10291-004-0104-8>.

660 Kotsakis, C. and M. Chatzinikos (2017) Rank defect analysis and the realization of proper  
661 singularity in normal equations of geodetic networks. *J Geod* 91: 627-652.  
662 <https://doi.org/10.1007/s00190-016-0989-3>.

663 Landskron, D. and J. Böhm (2018) VMF3/GPT3: refined discrete and empirical troposphere  
664 mapping functions. *J Geod* 91: 627-652. <https://doi.org/10.1007/s00190-017-1066-2>.

665 Legrand, J., N. Bergeot, C. Bruyninx, G. Wöppelmann, A. Santamaría-Gómez, M.-N. Bouin and  
666 Z. Altamimi (2012) Comparison of Regional and Global GNSS Positions, Velocities and  
667 Residual Time Series. In: Kenyon S., Pacino M., Marti U. (eds) *Geodesy for Planet Earth*.  
668 International Association of Geodesy Symposia, vol 136. Springer, Berlin, Heidelberg.  
669 [https://doi.org/10.1007/978-3-642-20338-1\\_12](https://doi.org/10.1007/978-3-642-20338-1_12).

670 Lyard, F., Lefevre, F., Letellier, T. and Francis, O. (2006) Modelling the global ocean tides:  
671 modern insights from FES2004. *Ocean Dynamics* 56: 394-  
672 415. <https://doi.org/10.1007/s10236-006-0086-x>.

673 Nishimura, T., H. Munekane and H. Yarai (2011) The 2011 off the Pacific coast of Tohoku  
674 Earthquake and its aftershocks observed by GEONET. *Earth planet Sp* 63 (22).  
675 <https://doi.org/10.5047/eps.2011.06.025>.

676 Petit G., Luzum B. (2013) The 2010 Reference Edition of the IERS Conventions. In: Altamimi Z.,  
677 Collilieux X. (eds) *Reference Frames for Applications in Geosciences*. International  
678 Association of Geodesy Symposia, vol 138. Springer, Berlin, Heidelberg.  
679 [https://doi.org/10.1007/978-3-642-32998-2\\_10](https://doi.org/10.1007/978-3-642-32998-2_10).

680 Petrie, E. J., M. A. King, P. Moore and D. A. Lavallée (2010) Higher-order ionospheric effects on  
681 the GPS reference frame and velocities. *J Geophys Res* 115: B03417.  
682 <https://doi.org/10.1029/2009JB006677>.

683 Rebischung, P., Z. Altamimi, J. Ray and B. Garayt (2016) The IGS contribution to ITRF2014. *J*  
684 *Geod* 90: 611-630. <https://doi.org/10.1007/s00190-016-0897-6>.

685 Rebischung, P., Z. Altamimi and T. Springer (2014) A collinearity diagnosis of the GNSS  
686 geocenter determination. *J Geod* 88: 65-85. <https://doi.org/10.1007/s00190-013-0669-5>.

687 Sagiya, T. (2004) A decade of GEONET: 1994–2003—The continuous GPS observation in Japan  
688 and its impact on earthquake studies. *Earth planet Sp* 56: xxix-xli.  
689 <https://doi.org/10.1186/BF03353077>.

690 Schmid, R., R. Dach, X. Collilieux, A. Jäggi, M. Schmitz and F. Dilssner (2015) Absolute IGS  
691 antenna phase center model igs08.atx: status and potential improvements. *J Geod* 90: 343-  
692 364. <https://doi.org/10.1007/s00190-015-0876-3>.

693 Tian, Y. and Z.-K. Shen (2016) Extracting the regional common-mode component of GPS station  
694 position time series from dense continuous network. *J. Geophys Res Solid Earth* 121: 1080-  
695 1096. <https://doi.org/10.1002/2015JB012253>.

696 Tobita, M. (2016) Combined logarithmic and exponential function model for fitting postseismic  
697 GNSS time series after 2011 Tohoku-Oki earthquake. *Earth Planet Sp* 68: 41.  
698 <https://doi.org/10.1186/s40623-016-0422-4>.

699 Tregoning, P. and C. Watson (2009) Atmospheric effects and spurious signals in GPS analyses. *J.*  
700 *Geophys Res Solid Earth* 114: B09403. <https://doi.org/10.1029/2009JB006344>.

701 Wang, M. and Shen, Z.-K. (2020) Present-day crustal deformation of continental China derived

702 from GPS and its tectonic implications. *Journal of Geophysical Research: Solid Earth*. 125.  
703 <https://doi.org/10.1029/2019JB018774>.

704 Wang, Q., P.-Z. Zhang, J. T. Freymueller, R. Bilham, K. M. Larson, X. a. Lai, X. You, Z. Niu, J.  
705 Wu, Y. Li, J. Liu, Z. Yang and Q. Chen (2001) Present-Day Crustal Deformation in China  
706 Constrained by Global Positioning System Measurements. *Science* 294(5542): 574-577.  
707 <https://doi.org/10.1126/science.1063647>.

708 Wdowinski, S., Y. Bock, J. Zhang, P. Fang and J. Genrich (1997) Southern California permanent  
709 GPS geodetic array: Spatial filtering of daily positions for estimating coseismic and  
710 postseismic displacements induced by the 1992 Landers earthquake. *J. Geophys Res*  
711 102(B8): 18057-18070. <https://doi.org/10.1029/97JB01378>.

712 Wu, W., Wu, J., Meng, G. (2018). A Study of Rank Defect and Network Effect in Processing the  
713 CMONOC Network on Bernese. *Remote Sens* 10(3): 357. <https://doi.org/10.3390/rs10030357>.

714 Zhan, W., F. Li, W. Hao and J. Yan (2017) Regional characteristics and influencing factors of  
715 seasonal vertical crustal motions in Yunnan, China. *Geophys J Int* 210(3): 1295-1304.  
716 <https://doi.org/10.1093/gji/ggx246>.

717 Zheng, G., H. Wang, T. J. Wright, Y. Lou, R. Zhang, W. Zhang, C. Shi, J. Huang and N. Wei  
718 (2017) Crustal Deformation in the India-Eurasia Collision Zone From 25 Years of GPS  
719 Measurements. *J. Geophys Res Solid Earth* 122: 9290-9312.  
720 <https://doi.org/10.1002/2017JB014465>.

721 Zou, R., Freymueller, J. T., K., Yang, S., and Wang Q. (2014) Evaluating seasonal loading models  
722 and their impact on global and regional reference frame alignment. *J. Geophys Res Solid*  
723 *Earth* 119:1337-1358. <https://doi.org/10.1002/2013JB010186>.

724

# Figures

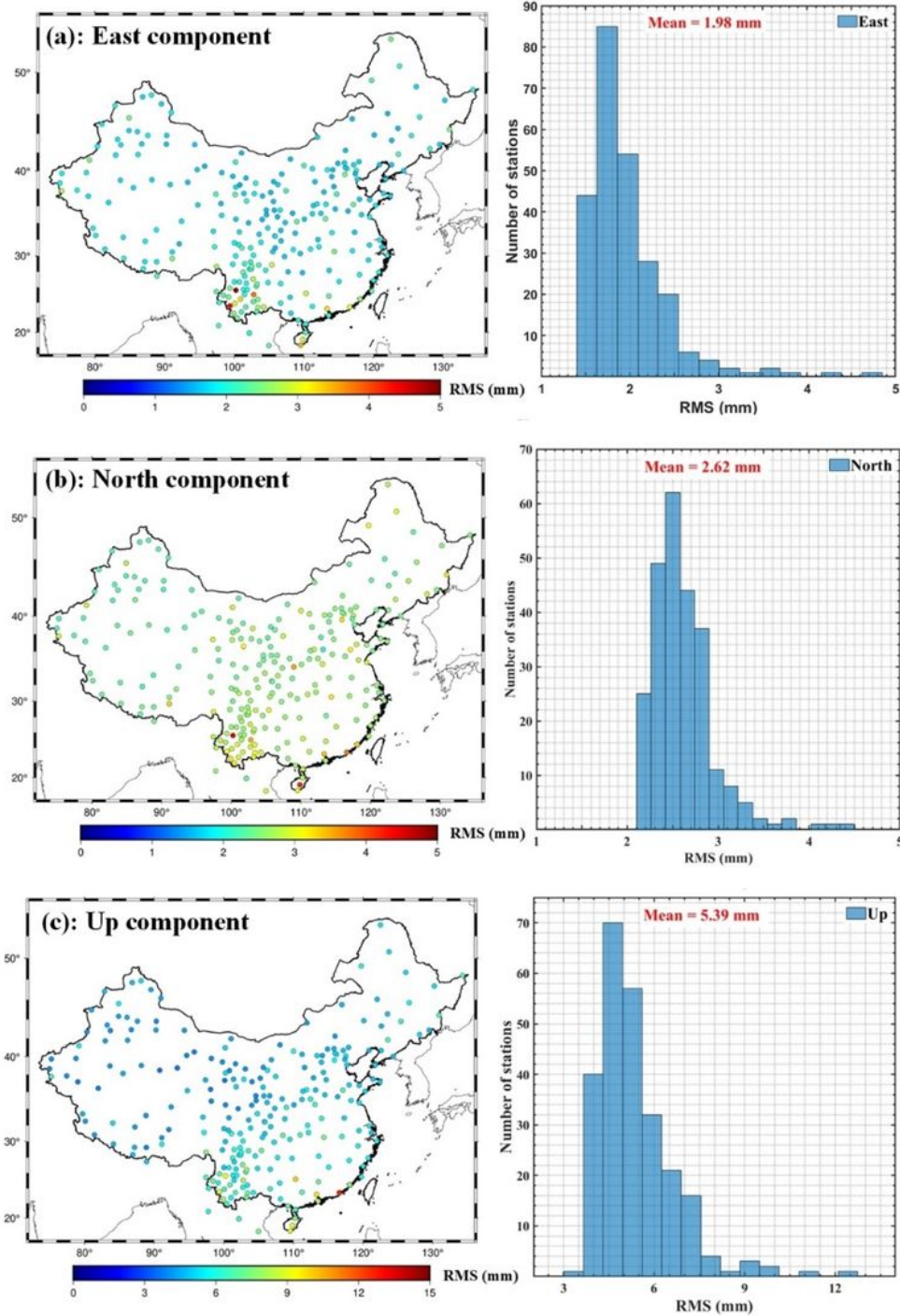
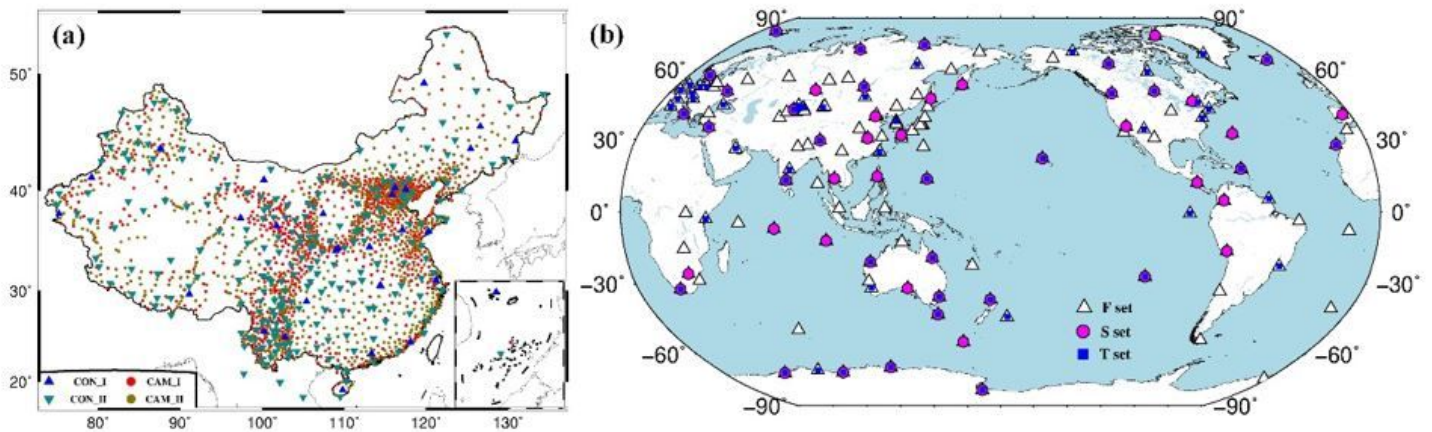


Figure 1

Statistic of RMS of raw coordinate time series for CMONOC GPS stations. (a) - (c) are for the east, north and up components, respectively. The left figures are spatial distributions and the right figures are histograms of the RMS respectively. Note: The designations employed and the presentation of the

material on this map do not imply the expression of any opinion whatsoever on the part of Research Square concerning the legal status of any country, territory, city or area or of its authorities, or concerning the delimitation of its frontiers or boundaries. This map has been provided by the authors.



**Figure 1**

The spatial distribution of our geodetic network. (a) is the spatial distribution of the CMONOC, with blue triangles being CON\_I continuous stations, dark cyan invert triangles being CON\_II continuous stations, red circles being CAM\_I campaign stations and dark gold circles being CAM\_II campaign stations, respectively; (b) is the spatial distribution of ITRF fiducial stations, with F set being the full set, S set being the stable set, and T set being the transformations set, respectively Note: The designations employed and the presentation of the material on this map do not imply the expression of any opinion whatsoever on the part of Research Square concerning the legal status of any country, territory, city or area or of its authorities, or concerning the delimitation of its frontiers or boundaries. This map has been provided by the authors.

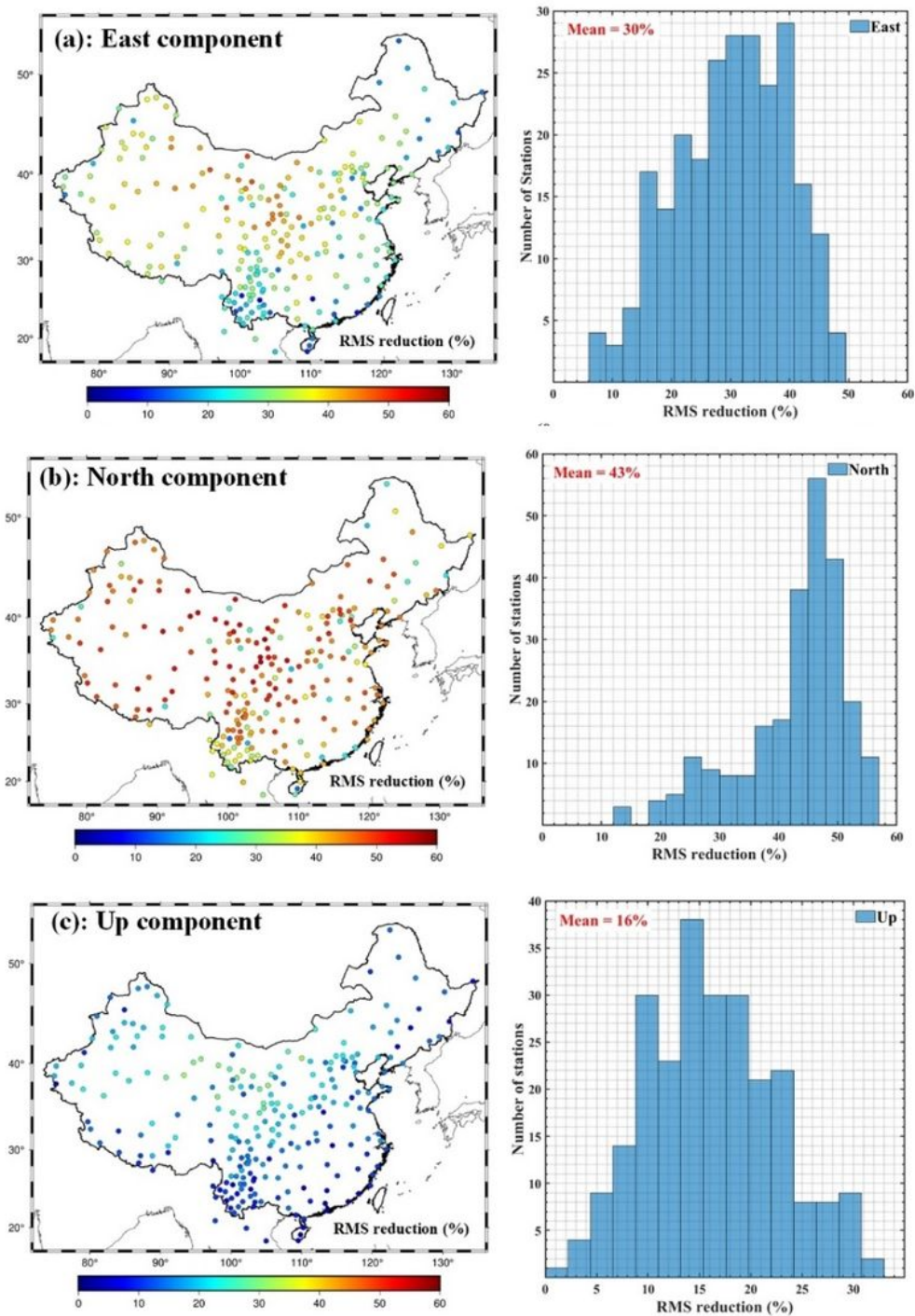


**Figure 1**

Statistic of the percentage of RMS reduction in the first-loop for CMONOC coordinate time series. (a) - (c) are respectively. The left figures are spatial distribution and the right figures are histograms of RMS reduction respectively. Note: The designations employed and the presentation of the material on this map do not imply the expression of any opinion whatsoever on the part of Research Square concerning the

legal status of any country, territory, city or area or of its authorities, or concerning the delimitation of its frontiers or boundaries. This map has been provided by the authors.

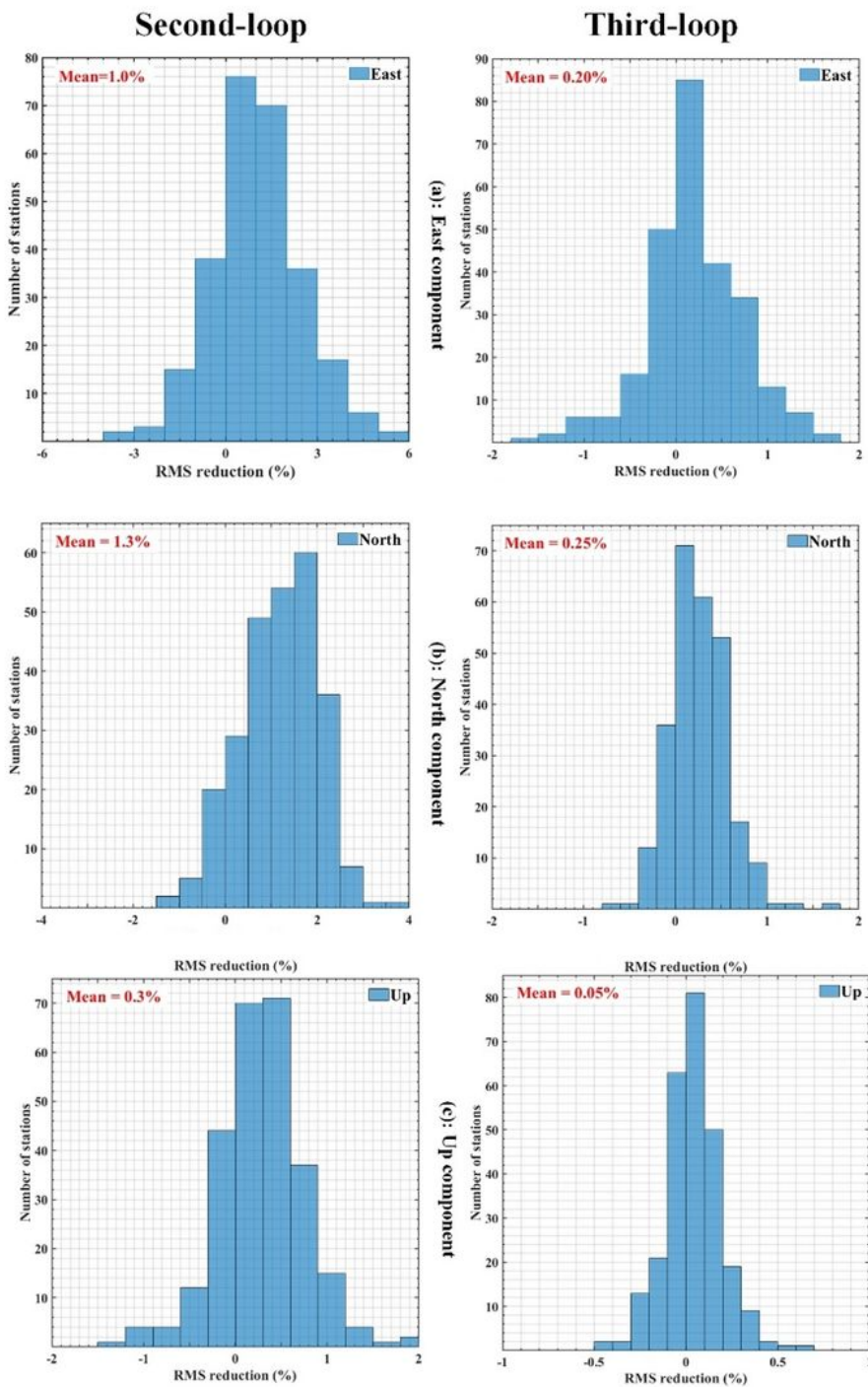


**Figure 1**

Statistic of the percentage of RMS reduction in the second- and third-loops for CMONOC coordinate time series. (a) - (c) are for the east, north and up components, respectively. The left figures are for the second-loop and right figures are for the third-loop. Note: The designations employed and the presentation of the

material on this map do not imply the expression of any opinion whatsoever on the part of Research Square concerning the legal status of any country, territory, city or area or of its authorities, or concerning the delimitation of its frontiers or boundaries. This map has been provided by the authors.

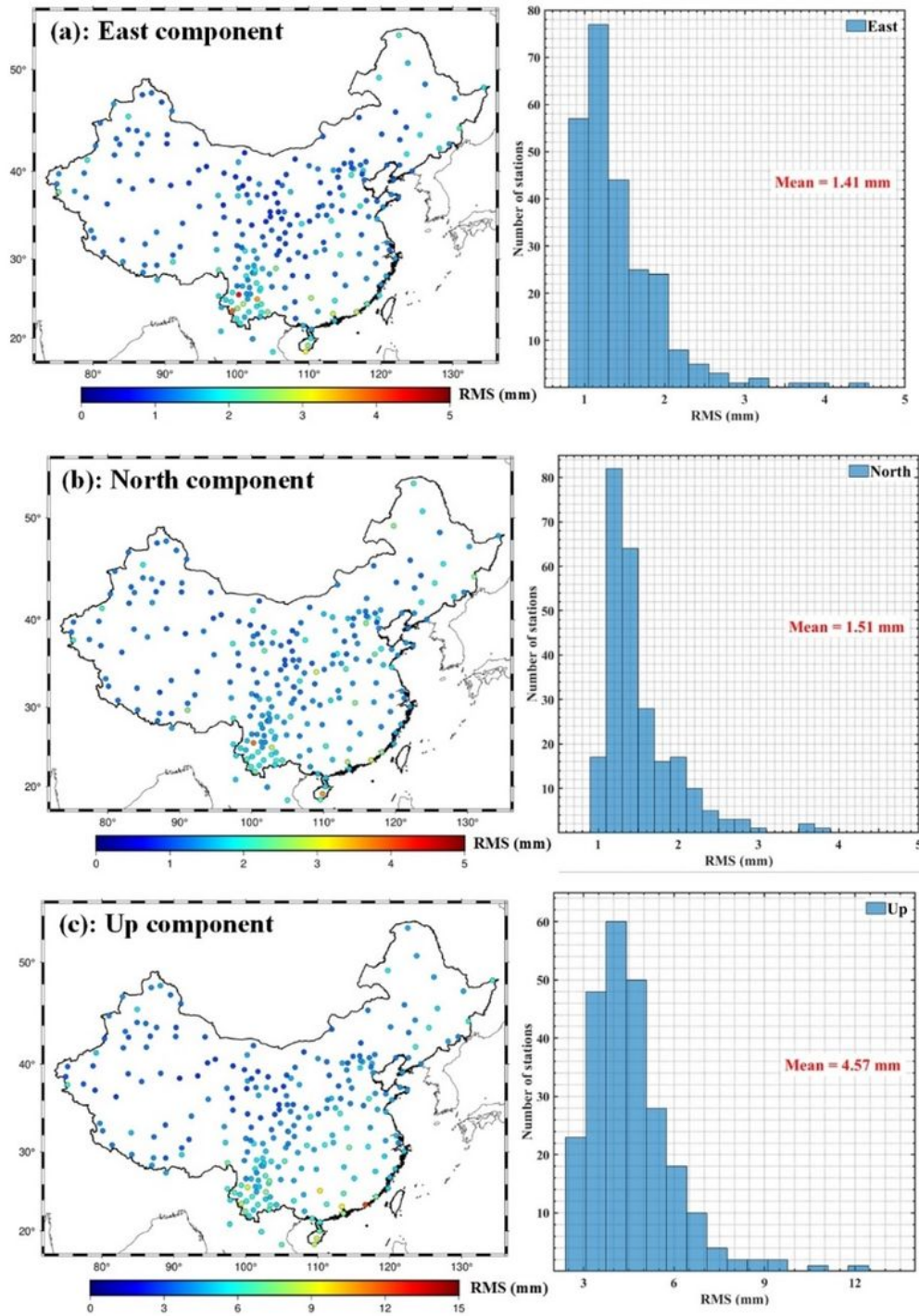


Figure 1

Statistic of RMS of the final coordinate time series for CMONOC GPS stations. (a) - (c) are for the east, north and up components, respectively. The left figures are spatial distributions and the right figures are

histograms of the RMS respectively. Note: The designations employed and the presentation of the material on this map do not imply the expression of any opinion whatsoever on the part of Research Square concerning the legal status of any country, territory, city or area or of its authorities, or concerning the delimitation of its frontiers or boundaries. This map has been provided by the authors.

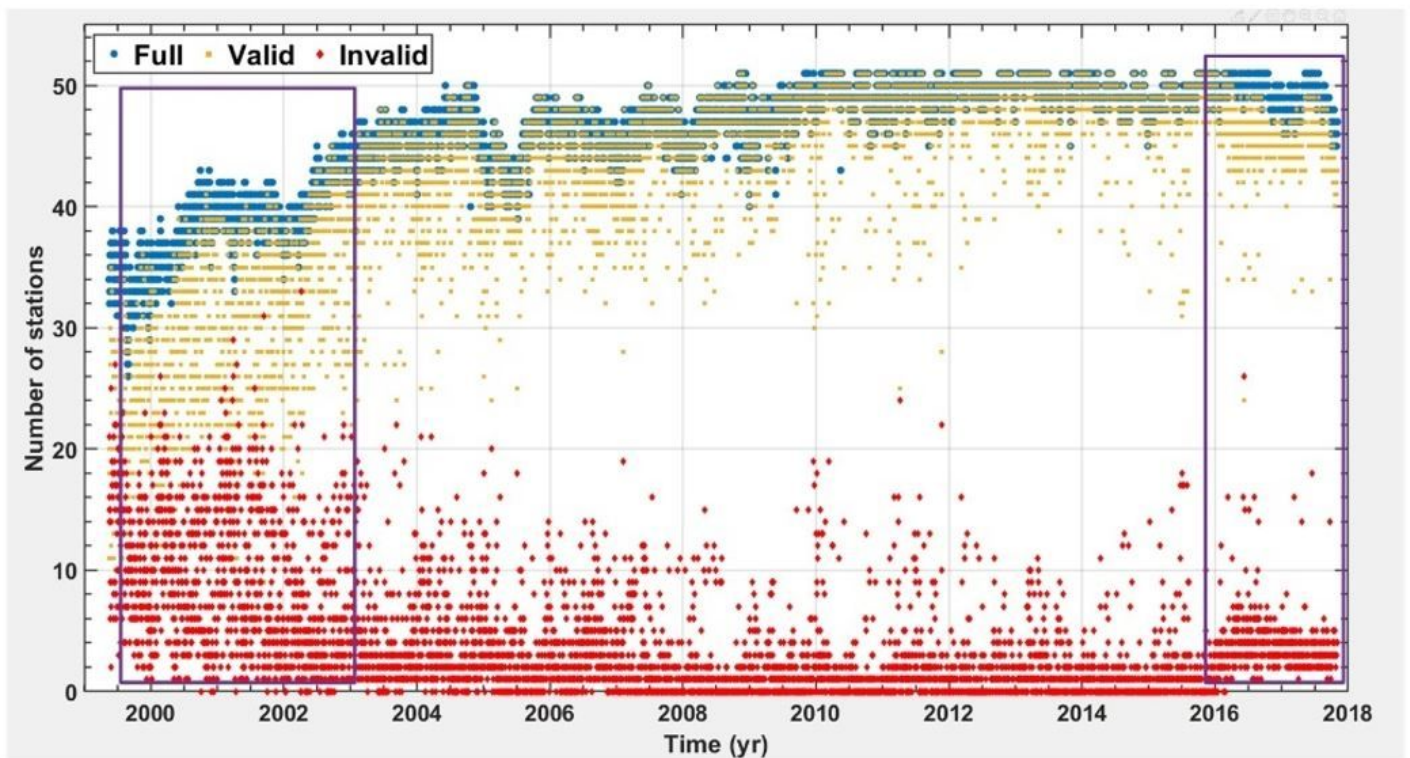


Figure 1

Statistic of the total number of fiducial stations in the conventional TRF realization of coordinates. The purple rectangles outline the shrinking periods.

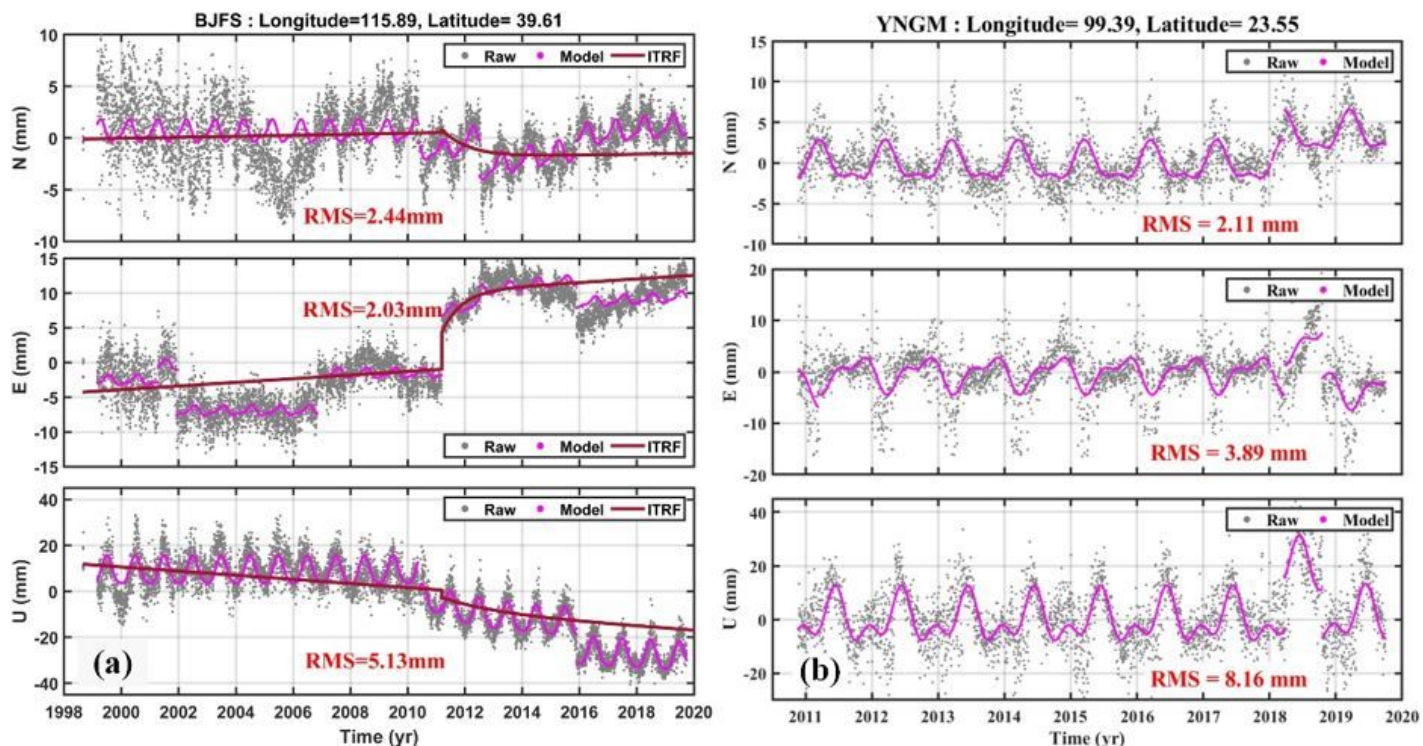


Figure 1

Detrended coordinate time series. (a) is for the CON\_I and ITRF fiducial station BJFS, (b) is for the CON\_I station YNGM. To view the time series, we subtract the secular trend signals from all three components, with the gray dots representing raw data, magenta dots representing the integral trajectory models employed in this study and brown lines representing ITRF2014 trajectory models.

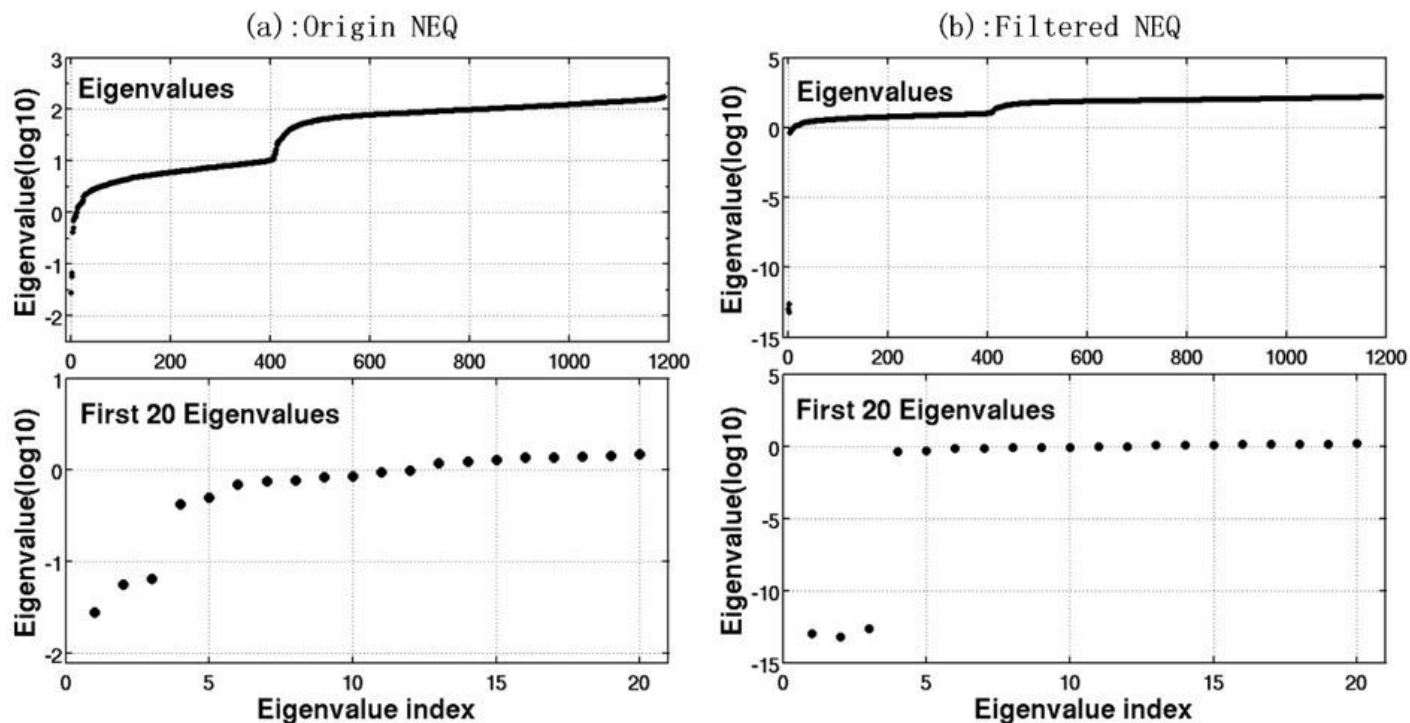
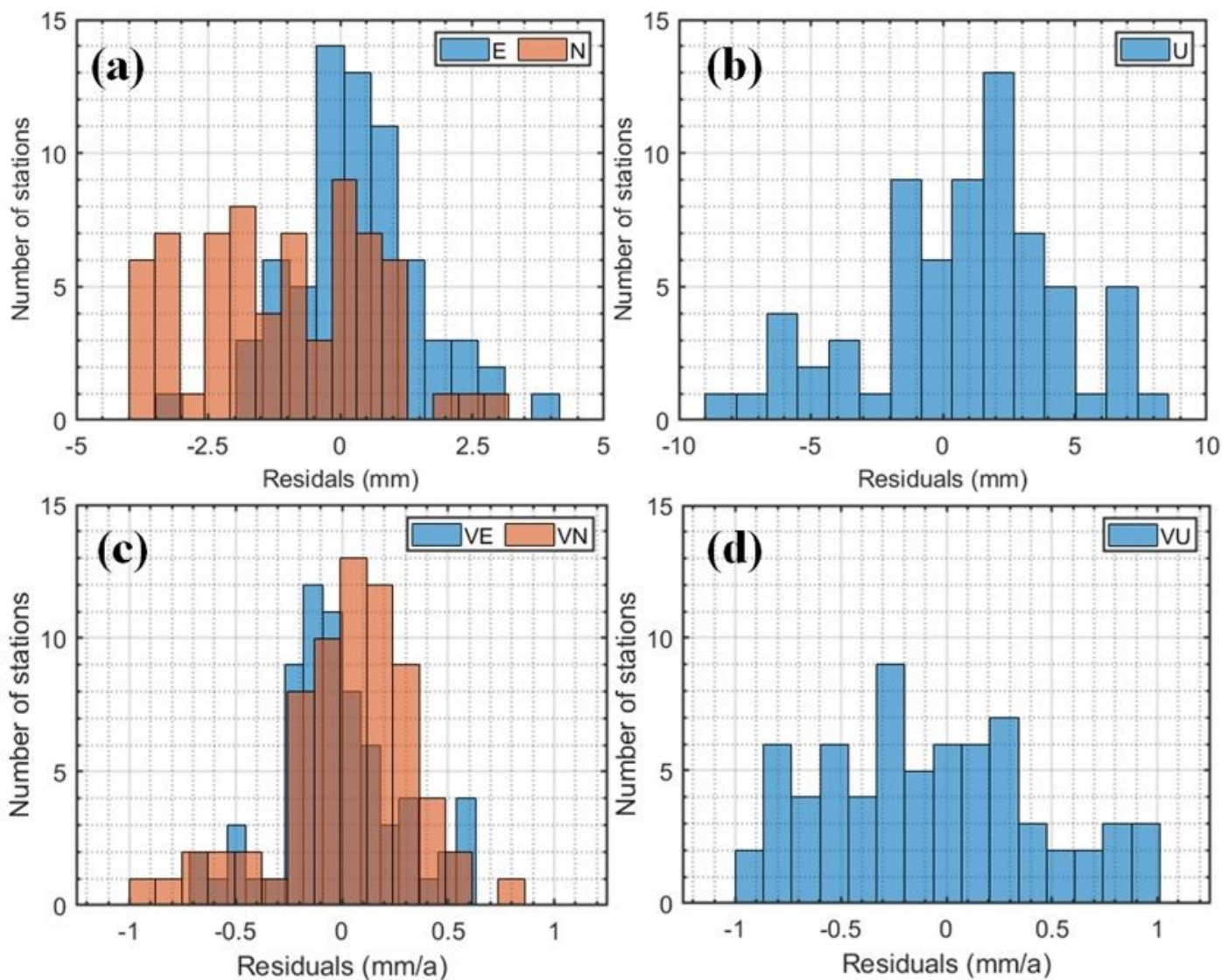


Figure 1

Eigenvalue property of the NEQ matrix on the 2014101. (a) is for the original NEQ matrix; (b) is for the frame-origin-related TRF contents filtered NEQ matrix, respectively.



**Figure 1**

Residuals of the Helmert transformation between the recursively defined TRF and the ITRF2014. (a) and (b) are residuals of station coordinates at epoch 2010.01.01 for horizontal and vertical directions, respectively, (c) and (d) are residuals of station velocities for horizontal and vertical directions, respectively.

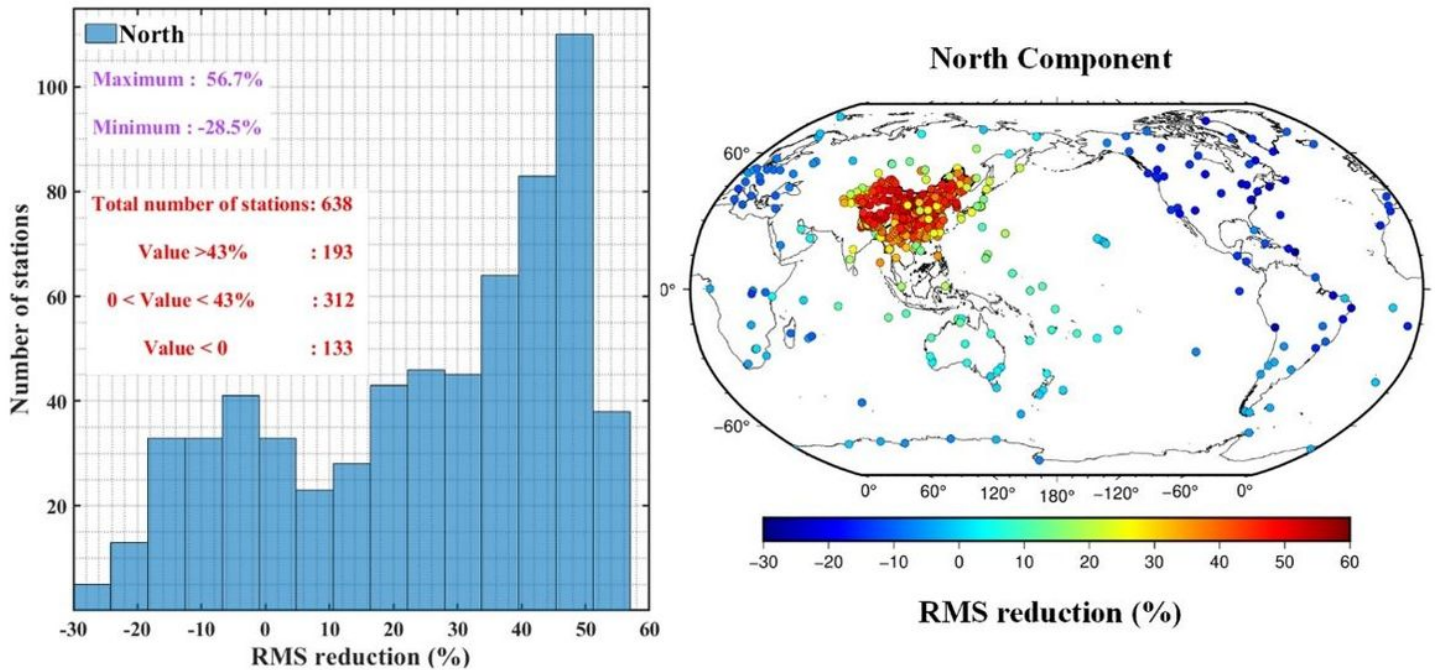


**Figure 10**

Statistic of RMS reduction for all GPS stations in the north component. The left figure is histogram of the percentage of RMS reduction, and the right figure is its spatial distribution. Note: The designations employed and the presentation of the material on this map do not imply the expression of any opinion whatsoever on the part of Research Square concerning the legal status of any country, territory, city or area or of its authorities, or concerning the delimitation of its frontiers or boundaries. This map has been provided by the authors.

## Supplementary Files

This is a list of supplementary files associated with this preprint. Click to download.

- [FiguresAbstract4.jpg](#)